Quantum mechanical modeling of the chemical reactivity of metal surfaces

two case studies involving water formation and dissociation

Thesis submitted for the degree of

Doctor Philosophiae in

Theory and Numerical Simulation of Condensed Matter

Candidate:

Antonio Suriano

Supervisor:

Prof. Stefano Baroni

February, 2007

To Tony Robbins, San Diego - CA

Contents

Introduction

The study of catalysis in chemistry dates back to the investigation of the fast reaction between H_2 and O_2 to produce water over a platinum surface, by Døbereiner [1] in the late 1823. The word *catalysis* was coined only later, in 1835, by Berzelius [2] to indicate the acceleration of a chemical reaction induced by the presence of a substance that remains chemically unchanged (the catalyst).

At the present time the term *catalysis* defines more generally the change in chemical reactivity occurring in the presence of a medium, called the catalyst, that does not modify reactants and products but, by acting on the intermediate states of a well specified reaction, increases or decreases the reaction rate, possibly determining the selectivity among different products.

The catalyst does not influence the thermodynamic equilibrium between reactants and products, but changes the speed of chemical reactions. The rate of many chemical reactions, k, follows a low empirically found by Arrhenius at the end of nineteenth century [3]:

$$k = \nu e^{-\frac{E_a}{k_B T}}, \tag{I.1}$$

where E_a is the so-called activation energy, T is the temperature, and k_B the Boltzmann constant. A catalyst modifies the rate acting on the activation energy. Many physical phenomena follow an exponential dependence upon the inverse of temperature (*e.g.* atmospheric pressure, cathodic current and electrostatic screening) and some of them are usually called *thermally*

activated processes.

We talk about *homogeneous catalysis* when the catalysts are in the same phases as the reactants (for example, a liquid solution) and *heterogeneous catalysis* when the catalysts are present in different phases (for example, a solid catalyst that activates reactions between gases). Heterogeneous catalysis is a surface phenomenon since it was soon realized that the easiest way to improve the efficiency was to increase the surface/volume ratio of the interface between catalyst and reactants, *e.g.* by decomposing the catalyst in a fine dust. Since late nineteenth century many catalytic reactions over surfaces have been studied [4] and practically applied to useful technologies such as, *e.g.* the Deacon process ($2HCl + \frac{1}{2}O_2 \rightarrow H_2O + Cl_2$), oxidation to SO_3, steam reforming of methane, methanol and ammonia synthesys and many others.

Heterogeneous catalysis

We could naively think that the best catalyst is the one that makes the reaction as fast as possible but this is not the case. The best catalyst is the one that works the way we expect, at the speed we need: an explosive reaction can be less interesting than a slow one. Also, a catalyst that accelerates unwanted reactions that may spoil (*poison*) the catalytic device is certainly noxious.

Schematically, a reaction catalyzed by a solid surface can be described by three elementary processes: adsorption of the reactants, formation of the products on the catalyst's surface, and desorption of the products.

Reactants form an activated complex, called the transition state, that decomposes into products. Transition state corresponds to a maximum in the energy profile plot from initial to final state. The height of the energy gap between transition state and initial state is called energy barrier and is equal

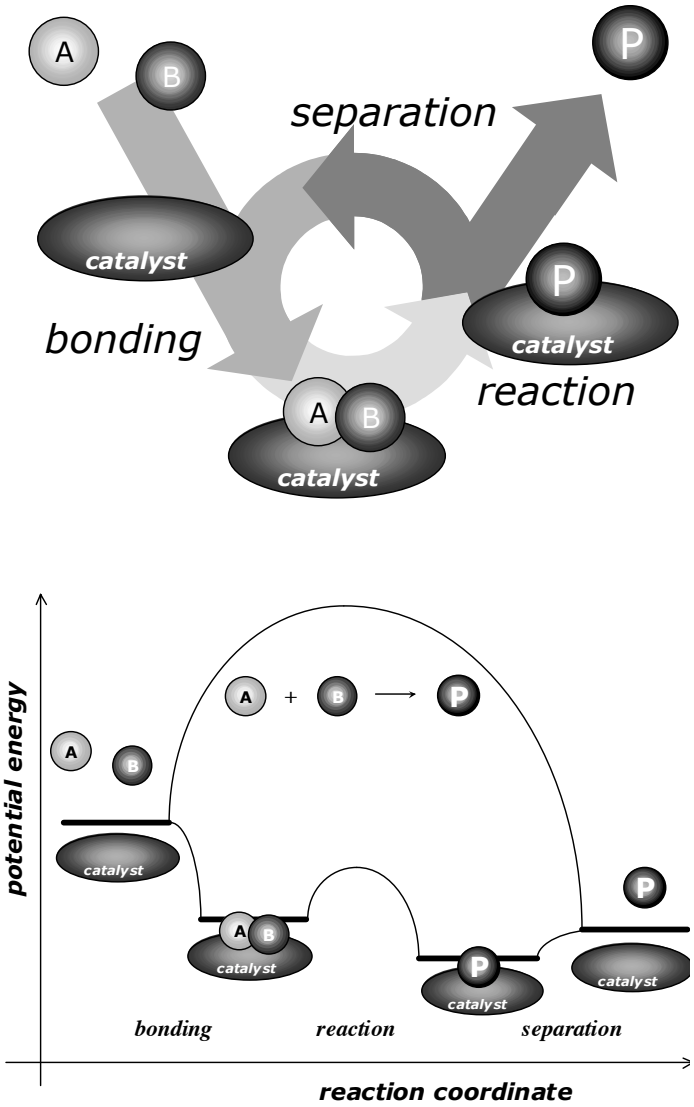

Figure I.1: A catalytic reaction on a surface consists in adsorption of reactants, formation of products and desorption.

to the activation energy present in Arrhenius' law (eq. (I.1)). A catalyst lowers energy barrier because of its major capability of binding transition states. A more reactive surface usually corresponds also to a higher binding energy of products. This slows down the overall reactivity because products do not desorb rapidly. A good catalyst must be designed as a compromise between the speed of reaction and the speed of desorption. This leads to the following practical statement called the *Sabatier's Principle*: for every catalytic reaction an optimum catalyst and optimum reaction conditions exist for which the interactions between adsorbed species and the surface of the catalyst is not too strong but not too weak either, such that the rate of reaction is maximum [5].

A typical way to picture the overall reactivity of a surface catalyst is a graph called Volcano curve [6]. In fact a volcano-shaped curve is obtained when we plot total reactivity (obtained experimentally) versus a parameter that is in relation to the strength of bonds of reactants, products or intermediates. The shape indicates that the best choice (as stated by Sabatier's principle) is a compromise between the two extremal behaviors [7]. It has been recently discovered that for dissociative chemisorption, adsorption energy and activation barrier are related with a linear relation that explains Sabatier's principle and volcano plots. This linear law is defined as the Brønsted-Evans-Polanyi relation and it depends mainly on the geometry of metallic surface and for simple molecules does not depend on adsorbate or metal [8].

A real boost to both experimental and theoretical studies of interfaces took place in the late fifties of last century because of ultrahigh vacuum systems development. For the first time real clean surfaces could be produced: it was possible to prepare surfaces and interfaces with a desired structure and controlled composition. All these technologies had a real impact in semiconductor solid-state device production and because of the importance of

electronics and computer science, they have improved fast. As a result it has been possible to study and characterize on the molecular scale many surface phenomena such as adsorption, bonding, oxidation, diffusion, desorption, phase transformation, transport, friction, electron scattering, and so on. Recent developments include relations with biological sciences and applications to organic materials aiming at the development of bio-compatible materials.

There are several experimental methods avaible to characterize the structure and other properties of the working catalysts [9]. These techniques can be classified in three types:

- spectroscopy giving information on the atomic short-range order: Surface Extended X-ray Absorption Fine Structure (SEXAFS), Photoelectron Diffraction (PhD), Electron and Photon Stimulated Desorption (ESD-PSD), X-ray Standing Waves, Ion Scattering Spectroscopy (ISS);

- diffraction techniques to probe the surface long-range order. This is the case of all diffraction experiments: Low Energy Electron Diffraction (LEED), Atomic or Molecular Beam Scattering, Grazing X-ray Diffraction;

- microscopes which give a direct access to the local atomic structure: High Resolution Scanning Electron Microscopy, Field Ion Microscopy (FIM), Scanning Tunnelling Microscopy (STM). In figure I.2 we can see a practical example of STM utility in understanding microscopic details of a reacting surface.

These different types of experiments have provided us with a wealth of detailed information about surface structures, adsorption geometries, bond strengths and elementary reactions steps.

A realistic heterogeneous catalyst consists in a disordered surface with many facets, defects, terraces with different behaviors among the various

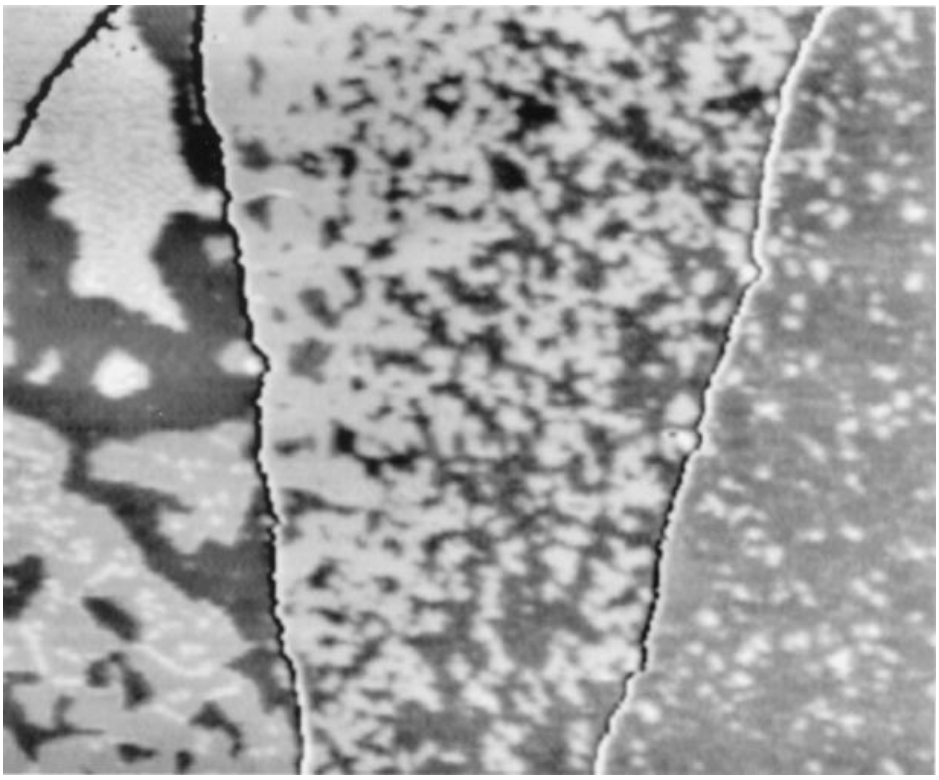

Figure I.2: Scanning tunnelling microscopy (STM) permits to have a clear description of microscopy structure of a metallic surface. In this STM image of a oxygen covered Pt(111) surface we clearly distinguish zones with different coverage of adsorbates (dark grey and white spots, species are oxygen and OH) and steps (dark lines). 1650Å $\times$ 1420Å [10]

pathways of a chemical reaction. Surface science approach to heterogeneous catalysis consists in isolating each component, by the production of perfect opportunely designed surfaces, and analysing the single contributions to the overall result. An outstanding example of the possibilities opened by surface-science technologies is the experiment by Dahl and others [11] about ammonia synthesis $N_2 + 3/2H_2 \rightarrow 2NH_3$ on Ru(0001). N_2 dissociation is really fast on steps as verified in the compared activation barriers between a golden poisoned surface and a regular one. Gold atoms deactivate low-coordinated step atoms and so reaction rate is determined only by active sites on terraces. As we can see in figure I.3 activation barrier results much lower when steps are active. Only the production of a pure artificial interface with well-designed steps, opportunely poisoned with few gold atoms has permitted to isolate the single reaction and to demonstrate the general trend about different reactivity of terraces and step atoms.

An important step toward a fundamental understanding of surface chemical processes is being made recently with the development of quantum theoretical methods to calculate equilibrium structures, adsorption energies, reaction paths, and activation energies for simple processes on metal surfaces. The accuracy of the resulting modeling is still not sufficient to predict rates of chemical reactions, but it is sufficient for a semi-quantitative description of adsorption and reaction processes and in particular for comparing and understanding chemical trends between different systems.

Theoretical modeling of surfaces

At the present time theoretical study of surface properties is achieved mainly through computational methods that practically consist in large-scale computer simulations of a set of atoms interacting and positioned in a defined space at our will. The choice of the parameters and conditions determin-

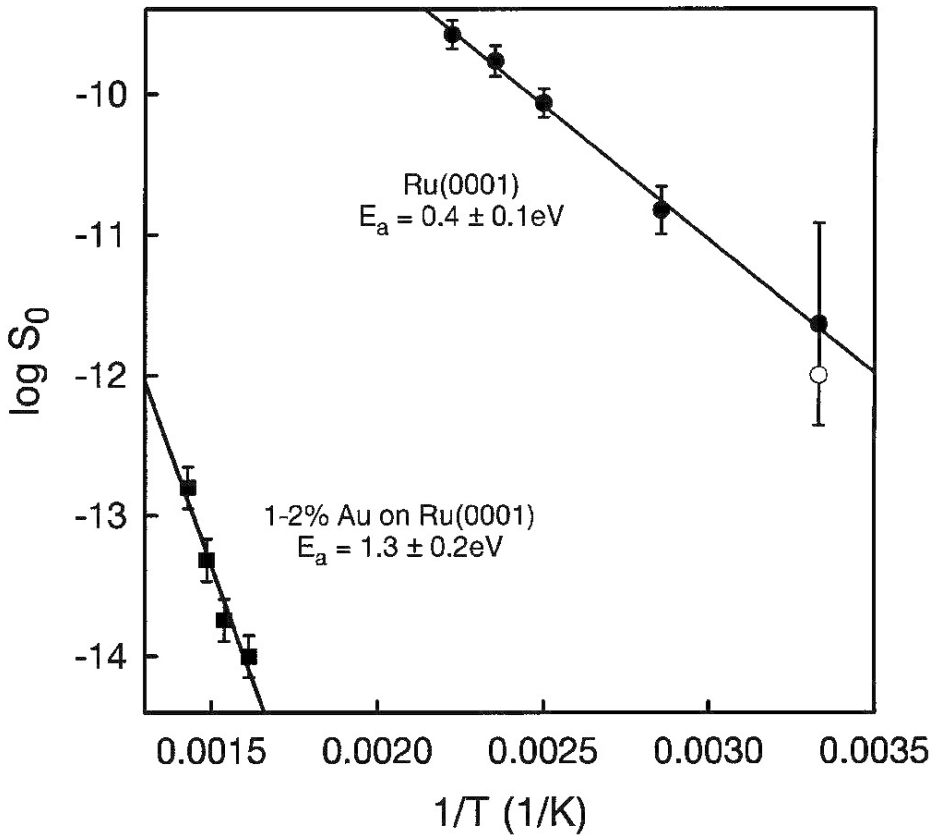

Figure I.3: An important experiment by Dahl and others [11] shows the change in reactivity for N_2 dissociation on a clean Ru(0001) surface, when we deactivate steps poisoning them with gold atoms. Energy barrier changes from 0.4 eV to 1.3 eV. This experiment shows clearly that steps and defects are sites with enhanced reactivity.

ing the simulation expands the range of systems we can treat with the only limit of the available computational resources. Numerical simulations can be performed in conditions that are not achievable experimentally such as, for example, very high pressure conditions, or to test different lattice constants without really straining the crystal.

Wave function based methods such as the inaccurate Hartree-Fock (HF) or the very accurate post-HF methods such as configuration interaction (CI), coupled cluster single & double (CCSD), many body perturbation theory (MBPT) [12] are, because of exponentially scaling algorithms used, computationally limited to systems of few electrons (10-100 electrons). If we consider metal atoms, as in our work, we can just compute systems of 10 atoms since each transition metal has on the order of 10 valence electrons.

In surface science we cannot use these computational demanding systems for structure of real interest but only for very little samples to be used as benchmark for Density Functional Theory (DFT) calculations. DFT describes how the ground state electron density and total energy can be obtained by solving a set of one-electron Schrödinger equations (the Kohn-Sham equations) instead of the complicated many-electron Schrödinger equation. This results in an enormous computational simplification, and systems with hundreds of atoms can be treated.

The combination of experimental and computational surface science methods has permitted the development, by Nørskov and others [13], of a simple and effective model of quantum mechanics of chemical interactions between metals and molecular adsorbates. A one electron state in an atom or molecule outside a metal surface will interact with all the valence states of the surface atoms [14]; these states form a band or several bands of states. Transition metals have usually one s electron in the metallic state and so the broad s band is half filled, while d bands are narrower.

Since d bands are narrow, the interaction of an adsorbate state with d

electrons of a surface often gives rise to bonding and anti-bonding states just as in a simple two-state problem. Instead when s band is involved the adsorbate states only broaden. This kind of bond is called *weak chemisorption* whereas when there are split-offs we refer to *strong chemisorption*.

Simple calculations [13, 14] demonstrate that if we just change the shape and positions of d bands of the surface metal, the chemical reactivity is modified. A practical generalization is that if the center of the d band is low compared to Fermi energy and meanwhile the band is broad, reactivity is lower and chemical bonds are weak. Instead the narrower the band is and upper near Fermi level the center of gravity is, much higher is reactivity and stronger the bonds. The general trend is that the farther to the left in the periodic table, the stronger the bond. Second, the farther down the periodic table, the weaker the interaction; the $5d$ metals are less reactive that $4d$ and $3d$ metals. Moreover the lower is atomic coordination, the narrower is d band and the higher is the center of gravity. This means that defects are usually much more reactive than clean surfaces (and this explains Dahl's experiment previously discussed). Bonds are stronger, transition states are lower in energies, adsorption sites can change and different kinds of reactions occur.

Water on transition metals

Water is perhaps the most important and most pervasive chemical of our planet. The influence of water permeates virtually all areas of biochemical, chemical and physical importance, and is especially evident in phenomena occurring at the interfaces of solid surfaces. The progress in understanding the properties of water on solid surfaces is evident both in areas for which surface science methodology has traditionally been strong (catalysis and electronic materials) and also in new areas not traditionally studied by surface

scientists such as electrochemistry, photoconversion, mineralogy, adhesion, sensors, atmospheric science.

Researchers in all these fields focused on very basic questions regarding the interactions of water with solid surfaces such as how is water adsorbed, what are the chemical and electrostatic forces that constitute the adsorbed layer, how is water thermally or not-thermally activated and how do coadsorbates influence these properties of water.

Water on transition metal surfaces is a topic studied since the dawn of catalysis because the first catalytic reaction was water formation on platinum, but it is still an open field for both theoretical and experimental studies. Theoretical modelling of ruthenium, platinum and rhodium surfaces through DFT calculations has permitted to investigate the variegate chemistry of water, including bonding at low coverages, wetting at high coverages, reaction steps for formation and dissociation in a large amount of recent publications to support experimental data coming from improving spectroscopy and microscopy techniques [15, 10, 16, 17].

Despite of the frenetic research in this field and the numerous progresses achieved, main issues are still open. For example a precise and definitive description of the complete kinetics for water formation over the surfaces at different temperatures [10] or the realistic structure for surface wetting at high coverages [18]. The progresses achieved in development of density functionals are not sufficient to definitely terminate the debates: little differences between computational data presented and the importance of van der Waals forces for reactions involving water do not permit the so called chemical accuracy required to consider predictive a pure computational result.

In this thesis we will present two different studies involving water reactions on transition metal surfaces. The first one involves study of water dissociation on flat and stepped platinum surfaces through the estimate of energy barriers for different reaction pathways. Data at the present time published

for DFT energy barriers calculations regard only the perfect clean Pt(111) that in our opinion can scarcely represent the behavior of a real surface on which reactivity is dominated by steps, defects, adatoms. The possibility of water dissociation on platinum surfaces determines the comprehension, not only of many useful catalytic reactions (water gas shift, steam reforming) and practical devices (fuel cells), but permits also to clarify a theoretical problem recently discussed such as surface wetting. Calculations reported are also a test of the general theory about dependence of reactivity in transition metals by Nørskov just presented. In fact we have compared energy barriers for water dissociation on clean Pt(111), stepped Pt(211) and Pt(311), showing the dependence of transition state energy versus the *d*-band center of gravity of differently coordinated atoms.

The second study was motivated by a collaboration with an experimental group working at ELETTRA. Experiments performed regard water formation over Rh(111) at different oxygen coverages to determine reaction mechanism between chemisorbed O and H, not yet fully understood [19]. Two different regimes for reactions occurring on Rh(111) in an hydrogen atmosphere sketched from experimental data open the way to several explanations. The most attractive concerns a possible route for hydrogen peroxide formation. Catalysts used at the present time to produce hydrogen peroxide are expensive and noxious [20] and many efforts have been done to determine the characteristics of a metallic surface adapt to activate the reaction [21, 22, 23]. Our results exclude this charming possibility for Rh(111) and explain experimental data by sketching two different regimes for the only water formation.

Plan of the work

In the first chapter we present numerical methods to describe termally activated processes and particularly the nudged elastic band method (NEB) to

find minimum energy paths (MEPs) on potential energy surface (PES).

In the second chapter we study a case that demonstrates by means of ab-initio calculations that steps are more reactive than plain surfaces. Water dissociation activation barrier is computed lower on stepped Pt(211) and Pt(311) surfaces respect to clean Pt(111) surface.

In the third chapter we investigate water formation on Rhodium surface at high oxygen coverage with the aim to explain an interesting experiment performed at ELETTRA - Trieste.

In the appendix A we make a brief discussion about density functionals and their drawbacks in correctly describing chemical reactions.

In the appendix B we briefly describe a parallel work of development and code maintenance of PWSCF code of suite ESPRESSO [24] with the purpose of adding exact exchange and hybrid functionals to the code.

Chapter 1

Computational methods

1.1 Quantum mechanics of chemical reactions

In the Born-Oppheneimer approximation nucleii in polyatomic systems are subject to an effective potential, $E(\mathbf{R})$ determined by the solution of the electronic problem:

$$\left(-\sum_{i=1}^{n}\frac{\hbar^2}{2m_e}\nabla^2_{\mathbf{r}_i}+\sum_{i<j}^{n}\frac{e^2}{|\mathbf{r}_i-\mathbf{r}_j|}-\sum_{i,j}^{n,N}\frac{Z_j e^2}{|\mathbf{r}_i-\mathbf{R}_j|}+\sum_{i<j}^{N}\frac{Z_i Z_j e^2}{|\mathbf{R}_i-\mathbf{R}_j|}\right)\psi_{\mathbf{R}}(\mathbf{r})=E(\mathbf{R})\,\psi_{\mathbf{R}}(\mathbf{r}), \tag{1.1}$$

$$\left(-\sum_{i=1}^{N}\frac{\hbar^2}{2M_i}\nabla^2_{\mathbf{R}_i}+E(\mathbf{R})\right)\Psi(\mathbf{R})=\mathcal{E}\Psi(\mathbf{R}), \tag{1.2}$$

in the assumption that we can consider electrons relaxed in their ground state. The stationary points of the effective potential $E(\mathbf{R})$, also called the Born-Oppheneimer potential energy surface (PES), determine the initial and final states of chemical reactions (local minima), as well as the transition states (saddle points) that separate the reactants from the products. All the efforts to solve and understand, by quantum mechanics first principles, the

chemistry of reactions are about finding electronic energies and sampling in the best way the PES.

Density functional theory (DFT) allows us to calculate the ground state energy of a system of interacting electrons, such as in equation (1.1), with a considerable numerical simplification respect to the usual many-body techniques. In fact Kohn-Sham theorems assert that, given an external potential V_{ext}, the knowledge of the ground state electronic density determines univocally all the properties of our system, and that it is possible to define a universal functional for the energy $E[n(\mathbf{r})]$ so that the ground state energy is the minimum value of $E[n(\mathbf{r})]$, achieved for the exact ground state density n_0 [25]. Practical implementation of DFT consists in solving a set of equations (Kohn-Sham equations) for an auxiliary system of non interacting particles, equivalent to the interacting one (this strong hypothesis is called the Kohn-Sham *ansatz*):

$$\left(-\frac{\hbar^2}{2m_e}\nabla^2_{\mathbf{r}_i} + V_{\text{ext}}(\mathbf{r}) + V_{\text{Hartree}}[n] + V_{\text{xc}}[n] + V_{\text{II}}\right)\phi_i(\mathbf{r}) = \epsilon_i\phi_i(\mathbf{r}) \quad (1.3)$$

$$n(\mathbf{r}) = \sum_i^n f_i \left|\phi_i(\mathbf{r})\right|^2 \quad (1.4)$$

where $\phi_i(\mathbf{r})$ are the KS eigen-functions with the corresponding occupancies f_i, V_{Hartree} is the Hartree potential, V_{II} is the ion-ion interaction, and V_{xc} is the exchange-correlation potential that includes all the many-body contributions. The density functional in KS *ansatz* has the form:

$$E[n(\mathbf{r})] = T_0[n(\mathbf{r})] + \int d\mathbf{r} V_{\text{ext}}(\mathbf{r})\, n(\mathbf{r}) + E_{\text{Hartree}}[n(\mathbf{r})] + E_{\text{xc}}[n(\mathbf{r})] + E_{\text{II}}, \quad (1.5)$$

where $T_0[n(\mathbf{r})]$ is the non interacting kinetic energy, E_{II} is the ion-ion interaction energy and $E_{\text{xc}}[n(\mathbf{r})]$ is the exchange-correlation energy that exactly defines $V_{\text{xc}} = \frac{\delta E_{\text{xc}}}{\delta n}$. Self consistent solution of (1.3) and (1.4) permits through (1.5) to finally obtain DFT ground state electronic energy. The vari-

ational nature of DFT allows us to compute the nuclear forces thanks to the Hellmann-Feynman theorem:

$$\mathbf{F}_I = -\frac{\partial E}{\partial \mathbf{R}_I} = -\int d\mathbf{r} n(\mathbf{r}) \frac{\partial V_{\text{ext}}}{\partial \mathbf{R}_I} - \frac{\partial V_{\text{II}}}{\partial \mathbf{R}_I}. \tag{1.6}$$

A set of numerical tools and methods has been developed to numerically solve KS equations for realistic systems. Calculations cannot describe all the atoms in a solid or a catalyst particle, and a strategy must be chosen to limit the number of atoms treated explicitly. We can choose between cluster methods and slab methods. In cluster methods we describe a portion of the surface in the form of a cluster, hoping that the size is sufficient to reproduce the local surface properties. In the slab method technique we use periodic boundary conditions to reproduce a super-cell with infinite replica along the surface plane. In this case we can use plane waves to expand wave functions and the basis set can be enlarged increasing cutoffs (we have two different cut offs, one for wave functions and one for charge density). Moreover a certain amount of slices of the solid are reproduced along the perpendicular direction in such a way to reproduce a real solid structure. The size of the super-cell along x and y directions (in the surface plane) must be chosen in such a way that adsorbates do not interact with their own periodic replica. A certain amount of vacuum in the z direction must be set in such a way that the interface resembles a real surface that in principle has half infinite vacuum. It is possible to reduce the errors due to the previous choices using a sufficient large supercell and vacuum space and a certain number of slabs to describe the surface.

A typical approximation consists in treating separately core electrons, whose contribution to chemical reactivity is negligible, through a pseudo-potential approach. First pseudo-potential proposed conserved the integral of charge density (norm conserving pseudopotentials) but this reduces the stability versus plane wave cut-offs that should be increased. Ultra-soft pseu-

dopotentials proposed by van der Bilt permit us to keep cut-offs reasonably low (see ref. [26]).

Numerical integrals over the Brilluoin zone are obtained through a sum over a mesh of k-points. For metals this approximation is extremely delicate since the abrupt change in occupancy near the Fermi surface can make the sampling inadeguate. Smearing techniques, such as the Methfessel-Paxton sampling that we have used [27], through the introduction of a low fictitious temperature enhance numerical stability for calculations involving metals.

Through an opportune preliminary tuning of all the parameters it is possible to achieve for energies obtained in DFT calculations over surfaces a numerical accuracy of about 1 mRy. Once we are in control of numerical errors caused by our model, all the responsibilities for the accuracy of our results depend from our density functional choice. Kohn Sham theorems indeed state that a density functional exists but gives no practical indication for the solution. None of the approximate density functionals proposed guarantees an adeguate description of all the possible systems. We refer to a detailed discussion about functionals in the appendices A and B but we just mention that the major drawbacks of standard functionals, that prevent chemical accuracy, consist in long-range dispersion forces (*e.g.* van der Waals) that miss completely, and in the lack of reliability for potential energy in the middle-range zone in which bonds usually break (*e.g.* in a transition state). Hybrid functionals, in which we mix an Hartree Fock exchange with other terms coming from LDA or GGA functionals, are the best technology available. Hybrid functionals are expensive in computational time and have not been used in our work but we have done the effort of implementing them in our code for future use (appendix B). After brief tests with LDA functionals we have switched to PBE [28] flavor of GGA for all the results here presented. All the calculations reported here have been done through plane wave DFT program PWscf contained in the ab initio Quantum ESPRESSO

distribution [24].

1.2 Thermally activated processes

To understand reactions from first principles calculations we have to find and characterize initial state (IS), final state (FS) and transition state (TS). These points are not subject to forces, since they are local minima on the PES (IS and FS) or saddle points (TS).

Knowledge of forces permits us to perform structural relaxations and damped dynamics to find local minima on the PES. Some of the best optimization algorithms are implemented in our code and for our relaxations we used BFGS algorithm [29]. Dynamics is instead not suitable to find transition states. Though the most intuitive approach to theoretical model a chemical reaction is to perform a molecular dynamics and find a trajectory leading from reactants to products, this way is impracticable and even wrong to estimate the rate k.

The transition from reactants to products is known to be a fast process (10^{-15} s) and what determines the overall rate is the probability of this event to occur. This particular kind of *rare events* is thermally activated and, as we'll show later, if we are far lower in temperature than activation energy, most of time in our trajectory is spent in a random walk near the initial state.

The best algorithm now used to perform quantum-mechanical molecular dynamics, in the context of density functional theory framework, is the Car-Parrinello method that allows us to reduce of an order of magnitude the computational effort respect to a single step of a typical structural relaxation. The length of the trajectory we need, τ, should be compared to the minimal time step necessary to an accurate dynamics, determined by the period of atomic vibrations (10^{-15} s). From Arrhenius formula we can have an estimate

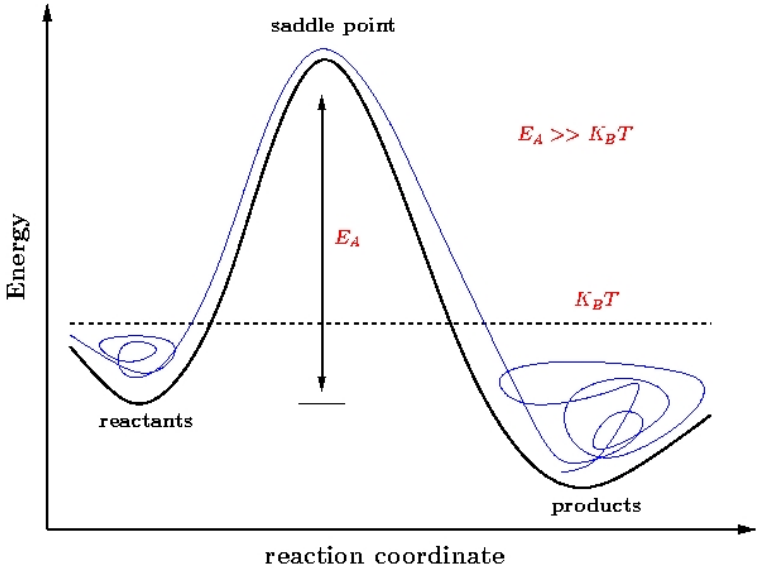

Figure 1.1: A one dimensional picture of a thermally activated process. For low temperatures the trajectory is concentrated near initial and final state and the transition is a rare event.

of τ for a typical reaction:

$$\tau = \nu^{-1} e^{\frac{E_a}{k_B T}}, \quad E_a \approx 0.5 \text{ eV}, \quad T \approx 300 \text{ K}, \quad \nu \approx 10^{13} \text{ s}^{-1} \rightarrow \tau \approx 10^{-4} \text{ s}. \tag{1.7}$$

The number of frames necessary to plot a single trajectory (10^{11} in our example) makes a Car-Parrinello simulation impossible.

In figure 1.1 we have a one dimensional example of our PES with two local minima and a saddle point (in 1-d graph it is a maximum) that are the positions in configurations space where we have reactants, products and transition state with three examples of trajectories at various temperatures. Our system oscillates nearby a local minimum for most of times with a frequency that does not depend upon temperature [30, 31] and in an harmonic approximation depends only by second derivative of PES. When it reaches the dividing surface between initial and final state (transition state), with

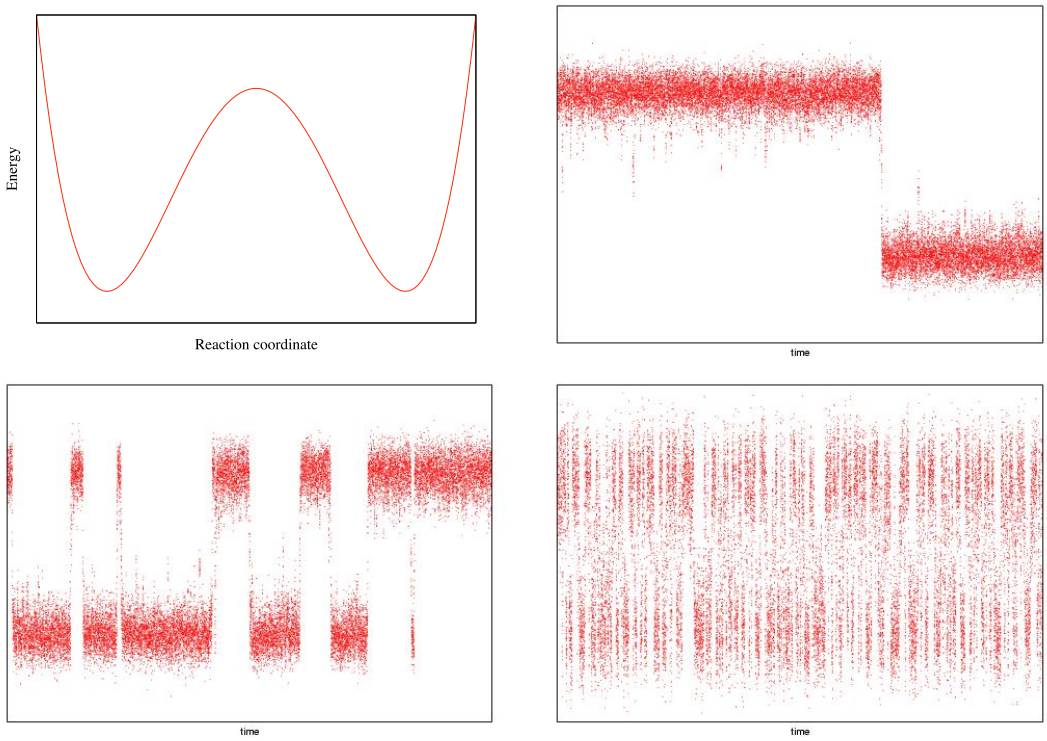

Figure 1.2: Simulation through Langevin dynamics of a thermally activated transition through a symmetric potential. Time evolution versus reaction coordinate are plotted in insets two, three and four for various temperatures.

a velocity pointing towards the other side, the reaction occur and it is an instantaneous process. In figure 1.2 we have plotted a simulation by mean of Langevin dynamics of a reaction going forward and backward many times through the symmetric potential, plot in first inset. The length of the period of time that the trajectory spends near initial or final state is not constant but its average determines the reaction rate. If we decrease temperature transitions become rarer, if we increase temperature transitions are frequent and the graph is confused cause the red points fill the square. The temperatures are in order $k_BT = 0.15E_a, \quad k_BT = 0.20E_a, \quad k_BT = 0.66E_a$.

The reaction rate is determined by the probability of being at the transition state with velocity pointing towards final state. In a one-dimensional picture like figure 1.1, and with the assumption that the PES can be approximated harmonically around initial state, we have that the rate is given by

$$k = \frac{1}{2\pi}\omega\left(q^{\mathrm{IS}}\right) e^{-\frac{E_a}{k_BT}}, \tag{1.8}$$

that needs to be generalized to multidimensional case. The prefactor ν is related to the shape of potential surface nearby the initial and saddle point [32]:

$$\nu = \frac{\prod_i^{3N} \omega\left(q^{\mathrm{IS}}\right)}{\prod_i^{3N-1} \omega\left(q^{\mathrm{TS}}\right)} \tag{1.9}$$

where $\omega\left(q^{\mathrm{TS}}\right)$ are the normal mode frequencies at initial state and transition state (in this case we have $3N-1$ normal modes because along reaction coordinate direction potential has imaginary frequency).

In this context it is useful to switch from newtonian mechanics to a discretized stochastic model in which all the other degrees of freedom take the role of a thermal bath. The equation of motion for a discretized path from initial state to transition state has a Langevin form:

$$\mathbf{r}_{i+1} = \mathbf{r}_i + \epsilon f\left(\mathbf{r}_i\right) + \xi_i \tag{1.10}$$

where ξ_i is a stochastic Wiener process without memory ($\langle \xi_i \rangle = 0$, $\langle \xi_i \xi_j \rangle = \sigma^2 = 4\delta_{ij}\epsilon k_B T (\gamma M)^{-1}$ and ϵ is the time discretization. For each discretized path we can find the probability density

$$P(\mathbf{r}_0, ..., \mathbf{r}_N) \propto e^{-\sum_{i=0}^{N-1} \frac{M\gamma |\mathbf{r}_{i+1} - \mathbf{r}_i - \epsilon f(\mathbf{r}_i)|^2}{4\epsilon k_B T}} P(\mathbf{r}_0) \tag{1.11}$$

that in the continuous limit, after an integration over all the possible intermediate steps, gives

$$P[\mathbf{r}(t)] \simeq e^{-\frac{S[\mathbf{r}(t)]}{2k_B T \gamma^{-1}}} e^{-\frac{V(\mathbf{r}_N)}{2k_B T}} e^{\frac{V(\mathbf{r}_0)}{2k_B T}} P(\mathbf{r}_0), \tag{1.12}$$

with the typical dependence of a thermal activated process versus the temperature and activation energy, where $S[x(t)]$ is the Langevin action

$$S[\mathbf{r}(t)] = \int \left[\frac{M}{2} \dot{\mathbf{r}}^2(t) + U(\mathbf{r}(t)) \right] dt \tag{1.13}$$

generated by a potential

$$U(\mathbf{r}) \propto -k_B T V''(\mathbf{r}) + \frac{1}{2} V'(\mathbf{r})^2. \tag{1.14}$$

We can define a maximum-probability path that, from equations above, is the one that minimizes Langevin action. In the limit of low temperature this reduces to the condition

$$\dot{\mathbf{r}} \propto \pm V'(\mathbf{r}), \tag{1.15}$$

that geometrically defines the path passing through the saddle points: the velocity is always tangent to the PES. This is called minimum energy path (MEP). In the next section we will describe an algorithm to find MEPs on the PES.

1.3 The Nudged Elastic Band method

A preliminary study of the PES permits to obtain local minima and to define the initial and final states. The MEP connects these two points passing

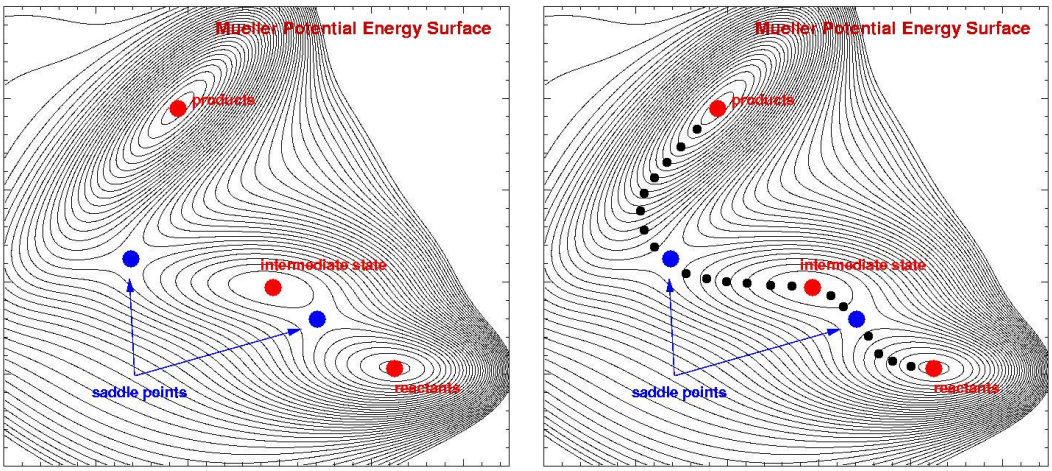

Figure 1.3: An example of a potential surface. We are looking for saddle points (blue spots), given an initial and final states (red spots). In this case the surface has also an intermediate minimum. In the second picture we have depicted the final result of a working algorithm. The sample well represents the MEP and we have images at each of the key points.

through the transition state (fig. 1.3). In order to find the MEP, we discretize a line on the PES through an adeguate number of points that we'll call images in our applications. In practice the number of images required to sample a reaction varies from five to about twenty.

We want to find paths, given the constraint of final and initial state, with the only estimate of energies and forces (first derivatives) and starting from a set of images representing a reasonable initial guess. The Nudged Elastic Band method, used for the calculation of all energy barriers in this thesis, and implemented in our Quantum ESPRESSO code[1] is a refinement of the Plain Elastic Band method (PEB) [24]. In the PEB [33] method each image is subjected to a force

$$\mathbf{F}_i = -\nabla V(\mathbf{r}_i) + \mathbf{F}_i^s, \tag{1.16}$$

where $\mathbf{F}_i^s$ is a spring correction:

$$\mathbf{F}_i^s = k_{i+1}(\mathbf{r}_{i+1} - \mathbf{r}_i) - k_i(\mathbf{r}_i - \mathbf{r}_{i-1}). \tag{1.17}$$

We link the images with elastic springs in such a way that they cannot collapse into initial and final states. Unfortunately the sampling obtained is thicker near local minima and sparser near transition state, where an increased accuracy is necessary.

The main idea of NEB method is to correct both the potential force and the spring force projecting it on tangent direction with an algorithm inspired by LUP method [34]:

$$\hat{\mathbf{q}}_i = \frac{\mathbf{r}_{i+1} - \mathbf{r}_i}{|\mathbf{r}_{i+1} - \mathbf{r}_i|}, \tag{1.18}$$

$$\mathbf{F}_i = -\nabla V(\mathbf{r}_i) + \hat{\mathbf{q}}_i(\nabla V(\mathbf{r}_i) \cdot \hat{\mathbf{q}}_i) + \hat{\mathbf{q}}_i(\mathbf{F}_i^s \cdot \hat{\mathbf{q}}_i). \tag{1.19}$$

The projection of the forces about convenient directions is called *nudging*.

[1] Both NEB and String methods have been implemented in our code by Carlo Sbraccia [31].

The projection of the potential perpendicularly to path maintains the distance between images also in the region near the transition state, where forces are strong. Image position versus reaction coordinate is determined only by spring elastic constants. In this picture estimate of energy barrier is still inaccurate because, even if the MEP is reached and images are well distributed, we have no guarantees that one of them reaches the maximum.

A solution is given by the climbing image technique [35]. We will describe the algorithm at the present time implemented in Quantum ESPRESSO. After we have done a sufficient number of NEB algorithm iterations, the shape of the MEP is quite well defined in our results. Before the end of the process we turn on a fictitious force on some chosen images to let them reach the maximum, and to prevent them sliding down away. The climbing images do not feel the springs at all and the potential force parallel to the path is reverted, in such a way that the climbing images are kicked on the top:

$$\mathbf{F}_i = -\nabla V\left(\mathbf{r}_i\right) + 2\hat{\mathbf{q}}_i\left(\nabla V\left(\mathbf{r}_i\right)\cdot\hat{\mathbf{q}}_i\right). \tag{1.20}$$

Chapter 2

Water on platinum (111) surfaces

After reviewing the importance of the chemistry of water on metal surfaces, this chapter contains the results of our study of water dissociation on Pt(111), with emphasis on the role of surface steps.

2.1 Chemistry of water on platinum

Fuel cells are really not new devices for electricity production, since they were invented by Sir William Grove in the middle of 19^{th} century [36], but they are considered very important for future developments of the technology for energy conversion against pollution. It is well known that nowadays huge amounts of electric power comes from oil and its derivatives that are responsible for the emission of large quantities of toxic gases, such as NO_x, SO_x, CO_2, CO, especially in urban areas because of their use as fuel. Fuel cells are foreseen to find applications in vehicles propulsion, batteries for portable devices (laptops, mobile phones), distributed and independent production of energy in large cities districts.

A cell is composed of two electrodes (anode and cathode) and the overall redox reaction is divided into two half-cell reactions, occurring at each electrode. The difference between potential of the two half-cell reactions gives the overall voltage. In fuel cells the two half-reactions involve oxygen reduction and hydrogen oxidation that combined give water formation:

$$H_2 + \frac{1}{2}O_2 \rightarrow H_2O. \tag{2.1}$$

Platinum can catalytically activate the reaction under the condition that CO is not present, because it would poison the catalyst. To purge CO from a H_2 mixture an interesting way is the so called water gas shift reaction:

$$CO + H_2O \rightarrow CO_2 + H_2 \tag{2.2}$$

that has a double interesting effect:

1. it purges CO from our gas, transforming it into an inert gas such as carbon dioxide;

2. it changes water (perhaps the same that we have as result of redox reaction in a fuel cell) into hydrogen, ready to be "burnt" in the cell.

The water gas shift reaction usually takes place at high temperature because it has an high activation barrier. Many different catalysts have been developed in order to reduce activation barrier, most of them formed by transition metals, alloys or their oxides such as Fe_3O_4, CuZn, ZnO [37, 38].

It is evident that water dissociation is an intermediate step for this important reaction. Steam reforming [39] of natural gas (methane, CH_4) is another technologically important example of single reaction involving water dissociation as an elementary step. Steam reforming is a large scale industrial reaction used to produce hydrogen as part of mixture composed of syngas (H_2 and CO in proportion of 2:1), carbon dioxide and water. The starting

reactants are water and methane and the most general form of the reaction is:

$$CH_4 + H_2O \rightarrow xCO + yCO_2 + zH_2 + wH_2O. \tag{2.3}$$

After some intermediate steps that include water gas shift we reach the desired syngas.

Syngas is also used to produce methanol over Cu/ZnO catalysts [30]:

$$CO + 2H_2 \rightarrow CH_3OH. \tag{2.4}$$

Methanol is not only present in a series of fuel cells, but it is also object of researches as a portable and secure source of hydrogen for little fuel cells. In fact a good reformer could be linked to a methanol source to obtain hydrogen to be consumed in the cell.

Platinum or water are present in most of rings of this chain (fuel cell, steam reforming, water gas shift, methanol production) and it is clear why a full comprehension of water behavior could help the fast development of better devices. Moreover, the formation of water and carbon dioxide is a concurrent channel for the direct catalytic oxidation of methane:

$$CH_4 + \frac{1}{2}O_2 \rightarrow CO + 2H_2, \quad CH_4 + 2O_2 \rightarrow CO_2 + 2H_2O. \tag{2.5}$$

All these examples show the importance of water dissociation reaction on platinum that consists of two fundamental steps: adsorption and dissociation on the surface. Regarding adsorption we remember that the conditions determining the wetting of the surface at high coverages [40] have attracted the attention of both experimentalists and theorists. In particular, it has been recently shown that hydroxyl (OH) would favor the formation of ordered layers of water on Pt, similarly to what happens on ruthenium [17, 41]. On ruthenium (0001) surfaces, in the past, two models have been considered: ice-like hexagonal structures, with water molecules binding alternatively through oxygen or hydrogen, and a buckled bilayer of molecules,

with a first layer directly bond to surface and the other one connected to the first by hydrogen bonds [18]. Nowadays researchers are moving to a model that contemplate a partial dissociation of water [15]. Both experimental and theoretical calculations aiming to distinguish between two forms of ice - like structure (buckled bilayer and flat ice) have been presented by Ogasawara and others in 2002 [17]. Finally some experimental data and DFT calculations by Feibelman (2003) support an exotic configuration with a $\sqrt{39} \times \sqrt{39}$ super-cell and partial dissociation of water with formation of H_3O and OH species between the majority of water molecules.

2.2 Water formation

As we have pointed in the first chapter fast oxidation of hydrogen into water was the first catalytic reaction studied since 19^{th} century from the pioneer discovery made by Dobereiner [1] in 1823. It is strange that still now our understanding of this process is rather incomplete.

Figures 2.1 and 2.2 report the results of a set of experiments performed by Volkening et al. [10] in 1998 in which direct microscopic information was obtained by the combination of scanning tunneling microscopy (STM) and high resolution electron energy loss spectroscopy (HREELS). The STM and HREELS experiments were performed in two separate ultrahigh vacuum systems. The HREEL spectrum in figure 2.1 exhibits mainly the vibrational modes of adsorbed OH, and demonstrate that reaction

$$O + H_2O \rightarrow 2OH, \tag{2.6}$$

leads to a pure OH layer. If the O layer was exposed to hydrogen instead of water, the resulting spectrum was dominated by H_2O and Pt-O modes. Results of these measures indicate that O, H, OH and H_2O are the only

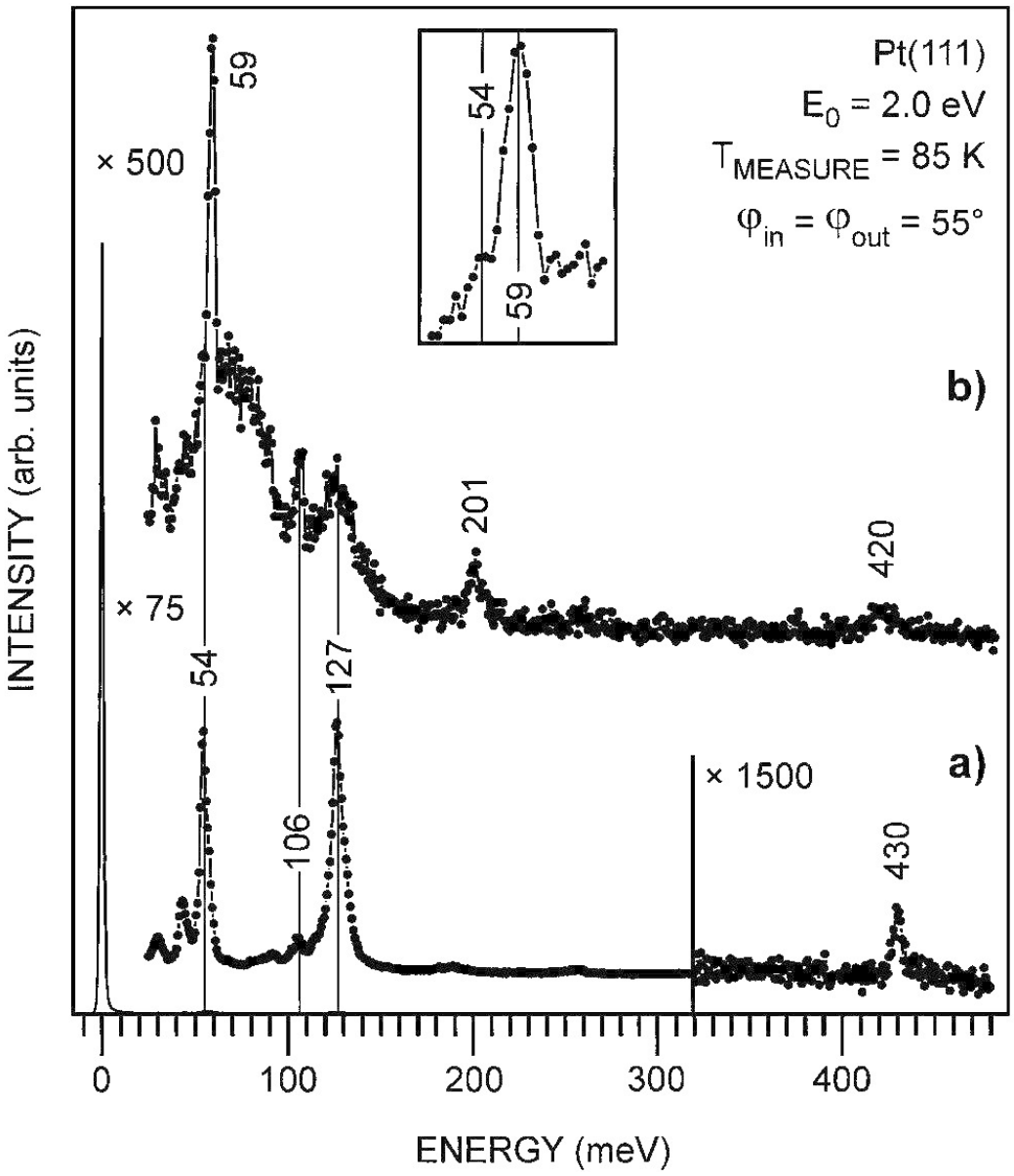

Figure 2.1: HREEL spectra from Pt(111), recorded after (a) annealing a coadsorbed layer of the 2×2 O structure and 1 L of H_2O at 170 K for 60 sec, and (b) exposure of 9 L of H_2 on the 2×2 O structure at 133 K and quenching to 85 K. (a) exhibits the vibrational modes of OH: the internal stretch mode (430 meV), the bending modes (127 and 106 meV), and the Pt-OH stretch mode (54 meV). (b) shows the main H_2O modes (internal stretch at 420 meV, scissors at 201 meV, libration at around 80 meV), the Pt-O stretch of O (59 meV), and modes of OH. Inset: Detail from spectrum (b). E_0 of the primary electrons and sensitivity factors as indicated; the incidence and exit angles ϕ_{in} and ϕ_{out} are referred to the surface normal [10].

species present on the surface and that the reaction

$$OH + H \rightarrow H_2O \tag{2.7}$$

is much faster than

$$O + H \rightarrow OH. \tag{2.8}$$

However, the series of STM images recorded during the reaction (Fig. 2.2) demonstrates that under identical conditions OH is by no means a short-lived surface species. Images taken on larger zones (Fig. I.2 at page 8) indicate the formation of OH spots and H_2O spots with fronts of reactions that clearly indicate formation of OH at the edge between H_2O spots and O spots. It is evident from experimental data that after hydrogen dissociation on surface, the first step should be an hydroxyl formation (2.8) but it seems that this in not always followed by the obvious reaction (2.7) also because of the not trivial dependence of reactivity versus temperature well known experimentally [42, 43, 44, 45]. It was found, for example, that the activation energy is higher for $T > 300\,K$ than for $T < 170\,K$ and that an induction period exists at low temperatures which is absent at higher temperatures [10].

On the other hand, the experiments by Volkening suggest, and first-principles calculations confirm [46, 47], that disproportionation reactions involving adsorbed water and atomic oxygen, such as, *e.g.* reaction (2.6), are likely to be catalyzed by the presence of a second, spectator, water molecule. Below the desorption temperature of molecular water from the metal surface, these reactions would thus provide an alternative route to the direct formation of OH from atomic O and H, which is the rate-limiting step of water formation at high temperature. For this reason, water formation on Pt(111) at low temperature has been described as an auto-catalytic process.

The barrier for water formation over a polycrystalline platinum foil was experimentally determined in 1992 using laser induced fluorescence [48]. The

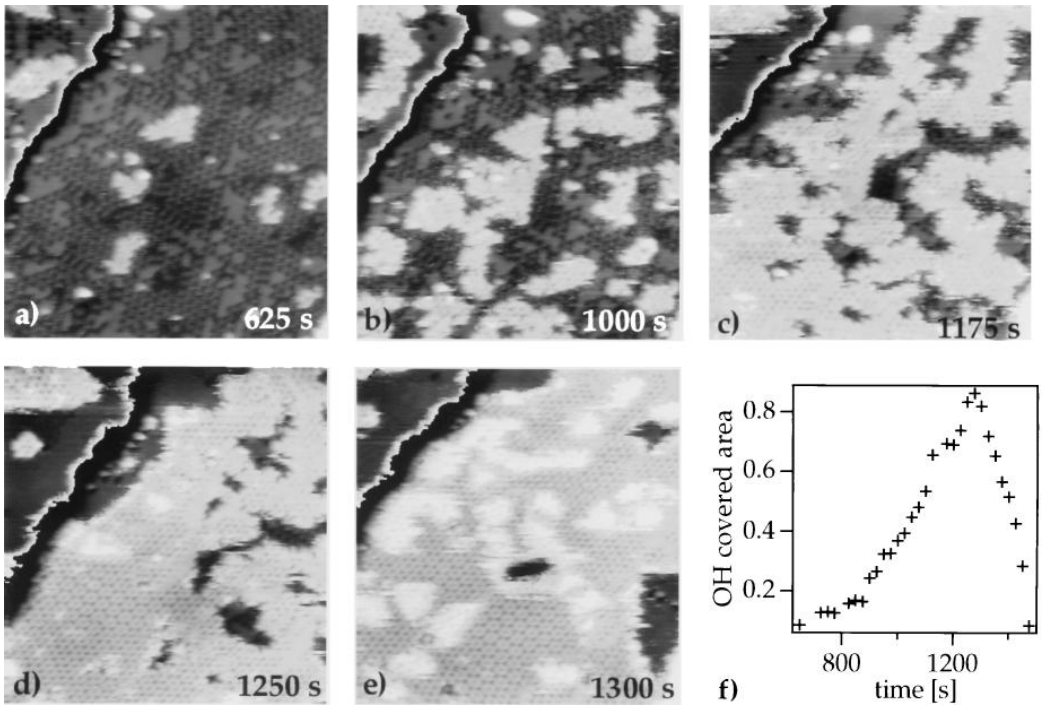

Figure 2.2: Series of STM images, recorded during hydrogen adsorption on a 2×2 O covered surface at T=131 Kelvin. The black and white line on the left is an atomic step [10]. In last picture OH covered area as a function of time.

formation and dissociation of water on Pt surfaces has been considered in a number of studies based on DFT [46, 47, 49]. In this chapter we re-address this problem with emphasis on the role of under-coordinated reaction sites occurring at steps in vicinal surfaces (such as (211) and (311)), an aspect which is of crucial importance for the reactivity of metal surfaces [13] and that has not been considered so far for the present system.

2.3 Water on Pt(111) surfaces

In this section our contribution to the study of water reaction on platinum surfaces is presented. DFT calculations performed include structural relaxations for the species on clean and stepped surfaces, and successive activation barrier estimate through NEB technique for water dissociation into hydrogen and hydroxyl on Pt(111), Pt(211) and Pt(311).

2.3.1 Preliminary calculations

Our DFT calculations have been performed in the plane-wave ultra-soft pseudopotential scheme [26], using the PWscf code of the Quantum ESPRESSO distribution [24], whereas molecular graphics has been realized with the XcrysDen package [50]. We have used the generalized-gradient exchange-correlation functional of Perdew, Burke, and Ernzerhof (PBE) [51]. The atomic ultra-soft pseudopotentials used in this thesis can be found in the PWscf pseudopotential table publicly available [52]. To ensure mRy consistency, we have adopted a kinetic-energy cutoff of 30 Ry for the wave functions and of 200 Ry for electron charge-density distribution. Molecular adsorption on the (111), (211), and (311) surfaces has been modeled using four-slab supercells with a vacuum region of 10 Å separating two adjacent slabs. The two topmost layers were allowed to relax so as to minimize the surface energy, while the other two have been kept fixed at the bulk interatomic distance. Brillouin-zone integrations have been performed with the Gaussian-smearing special-point technique of Methfessel and Paxton [27], using a first-order smearing function with a width of 0.02 Ry. For each of the supercells considered here, we have used k-point grids equivalent to the $8\times8\times8$ Monkhorst-Pack set in the bulk. Spin-polarization effects were found to be negligible, and have thus been consistently neglected. Equilibrium geometries of reactants and products have been determined by minimizing the

energy of the system, while reaction barriers have been determined using the climbing-image NEB described in chapter 1, with 9 system images per path, including the extremes. For each reaction studied here several paths have been sampled, but only the one yielding the lowest barrier is reported and discussed. Platinum is a face-centered cubic metal with a lattice parameter of 3.92 Å [53] and a bulk modulus of 230 GPa to be compared with our predictions of 3.99 Å and 230 GPa, respectively. Our predicted bond length and bond angle for the water molecule in the gas phase are 0.97 Å and 104.3 degrees, respectively, to be compared with experimental values of 0.96 Å [54] and 104.5 degrees [55]. Relaxation for the clean surface was predicted to be +0.9% for d_{12}, in agreement with experiments and previous theoretical studies [56, 57]. Our calculated value for the surface energy is 7.1 mRy/Å^2 to be compared with an experimental value is 11.7 mRy/Å^2 [58].

2.3.2 Water on clean Pt(111)

The potential-energy landscape for water, hydrogen, and for the hydroxyl group on the Pt(111) surface has been investigated using 3×3 supercells, corresponding to a nominal coverage $\theta = 0.11$ monolayers (ML). Comparison with calculations made for 2×2 supercells ($\theta = 0.25$ ML) shows that our chosen size of the supercell is adequate to guarantee mRy accuracy on the adsorption energies of the isolated H, OH, and H_2O species. Some of the calculated adsorption energies and geometries are reported in Figure 2.3. Water molecules bind weakly to the metal surface, the small binding energy being largely affected by dispersion forces, which are not properly accounted for in our DFT-GGA approach, as discussed in appendix A. This being said, our calculations predict the top site to be the most favorable for water adsorption, with the molecular plane parallel to the metal surface, and the molecular geometry almost unchanged with respect to the gas phase. The

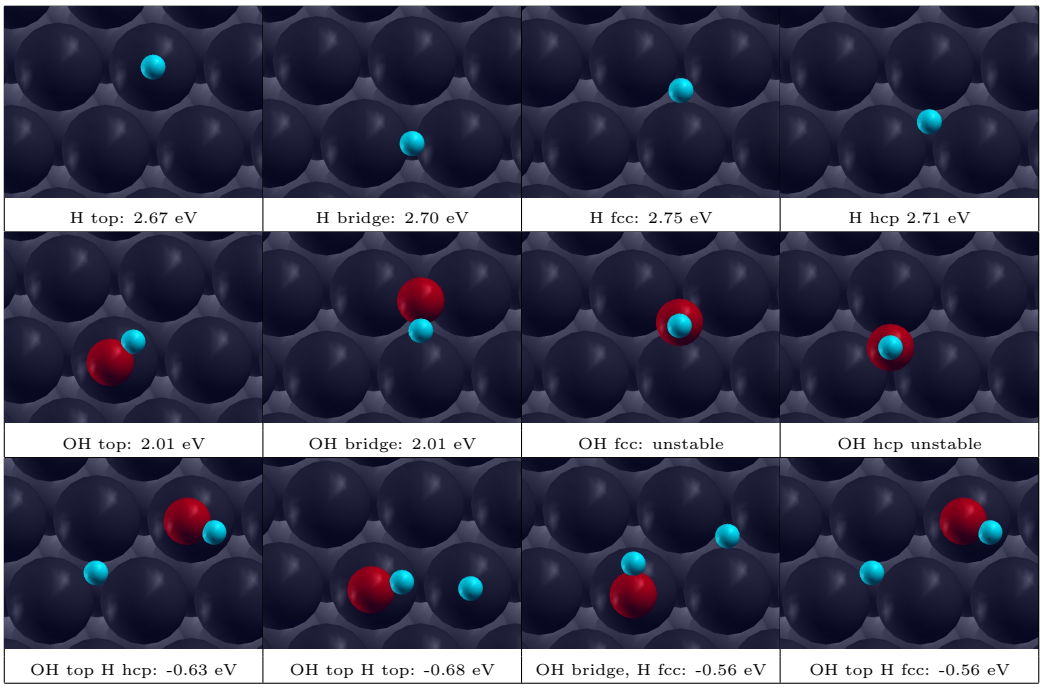

Figure 2.3: Adsorption energies for H and OH on Pt(111). For H and OH the energy is referred to the free surface plus the adsorbed species in the gas phase (H in gas phase is spin polarized). For the products pair (OH + H) the reference is the water molecule in the gas phase, plus the clean surface. In all pictures of this chapter periodic replica of adsorbed species are removed.

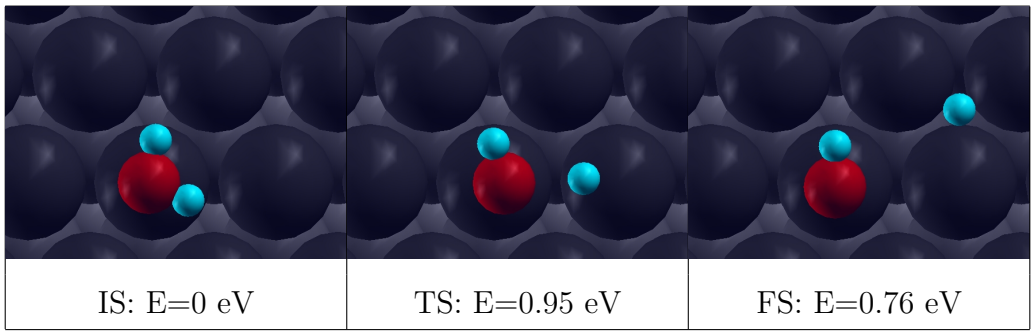

Figure 2.4: Images of initial, transition, and final states for water dissociation on Pt(111). The minimum energy path has been calculated with the NEB technique using 9 images.

resulting adsorption energy is 0.20 eV, at our (admittedly inaccurate in this case) DFT-PBE level. This value is lower than predicted by Michaelides and Hu [46], who find a binding energy of 340 meV, corresponding to adsorption at a bridge site; Karlberg et al. [47] find a binding energy of 280 meV corresponding to a top adsorption site, whereas measurements by Hickman and Schmidt [39] and Williams, Marks, and Schmidt [48] give a value of 470 meV. We believe that our conclusions on the dissociation mechanism and its dependence on the local coordination of the reaction site depend little on this inaccuracy which should only affect the diffusion of water molecules among different adsorption sites in the initial state.

The on-top and bridge adsorption sites of OH are predicted to be almost degenerate, whereas H atoms are predicted to bind preferentially at FCC hollow sites. On-top OH binds through O with an O-Pt distance of 2.0 Å, forming an angle of 106 degrees with surface. The equilibrium distance of adsorbed H atoms from the first Pt layer is 3.2 Å. Some of the significant final (OH + H) states of dissociation are also reported. We notice that water dissociation on Pt surfaces is endothermic, as the energy of the most stable configuration for the H+OH pair is about half eV higher than for the molecule in the gas phase. Minimum-energy paths have been searched for reactions proceeding from the water-on-top to the OH on- top/H-fcc configurations (see figure 2.3). In Fig. 2.4 we report the initial (IS), final (FS), and transition (TS) states of the MEP thus found. Inspection of Fig. 2.4 shows that water dissociation is a late transition state reaction whose TS is very close to the FS, and its energy mainly determined by the breaking of an OH bond. The energy difference between the TS and the FS is mainly due to the diffusion of H away from the reaction center. The only differences that we found among several MEP's are just due to the different H diffusion pathways from the TS to the FS. The calculated activation barrier is 0.95 eV for the forward reaction and 0.19 eV for the inverse one. A similar cal-

culation performed for a FS with the OH radical at a bridge site, which is predicted to be degenerate with OH on-top (see Fig. 2.3), gave a slightly larger (90 meV) activation barrier. The transition state is very simple, being characterized by the breaking of an OH bond with H moving away in the direction of its stable site in the final state. The data found in the literature for this process are different from ours and also scattered among themselves. Michaelides and Hu [46] (MH) find 680 meV for the direct and 210 meV for the inverse barriers. The value for the inverse barrier is very close to ours. It is tempting to attribute the discrepancy for the direct barrier to the numerical approximations made by MH who neglect atomic relaxation in the metal slab and also estimate the transition state with a constrained minimization technique. In fact, when releasing the first approximation, their estimate of the reaction barrier increases from 680 to 770 meV, recovering one third of the discrepancy with respect to our calculations. It seems to us, however, that allowing for atomic relaxation in the substrate should affect the TS state more than the IS where a water molecule is weakly bound to the substrate, and lower the energy of the TS more than that of the IS, thus decreasing rather than increasing the estimated energy barrier. A similar reasoning would also suggest that an improved algorithm for locating the TS could only decrease the estimate of the reaction barrier. Wilke et al. [49] report a value for the forward reaction of about 690 meV, almost equal to that for the reverse reaction, corresponding to an estimated substantial degeneracy between the molecular and dissociated species of water on Pt(111). Experiments [39] seem to indicate 1600 meV for direct barrier and 650 meV for inverse barrier, corresponding to an energy difference between dissociated and undissociated adsorbed water molecule of 950 meV.

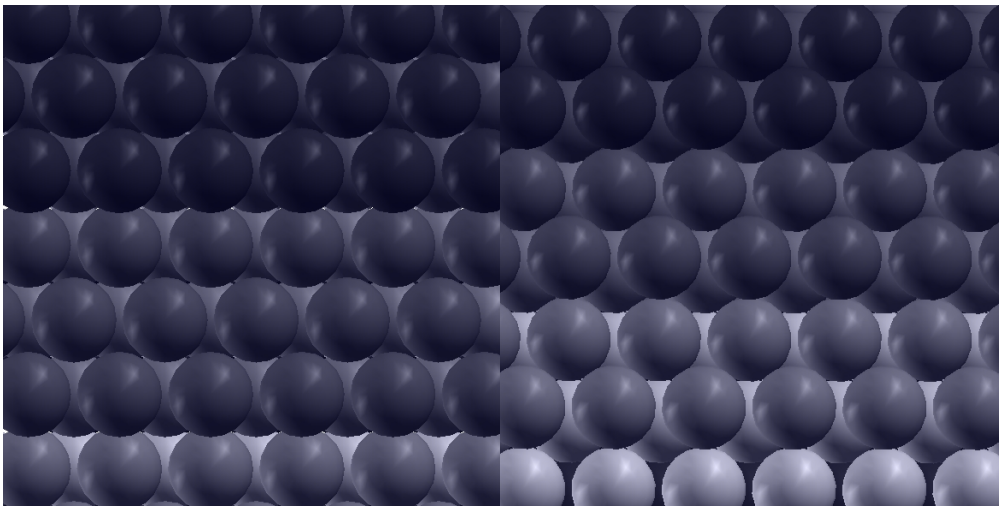

Figure 2.5: (211) and (311) surface in a top view. The colors of these images are chosen to enhance (111) terraces and (100) steps.

2.3.3 Water on stepped surfaces

Experiments by Dahl and theoretical modeling by Nørskov, presented in the introduction, confirm the well known property that the reactivity of metal surfaces strongly depends on the local coordination of the active reaction sites [17, 11, 59]. In order to investigate the effect of the local coordination in the present case, we have calculated the reaction barriers for water dissociation occurring at steps in vicinal (211) and (311) surfaces (see Fig. 2.5). Our supercells are chosen in this case so as to allow a distance of 3 Pt-Pt bond lengths between periodic images along the direction parallel to the steps. Bulk atoms in FCC lattices are 12-fold coordinated; atoms at clean (111) surfaces have coordination 9, whereas atoms at (001) steps in (111) surfaces are 7-fold coordinated. Lower coordination implies a smaller width of the d-projected local density of states (d-PDOS), as well as an upward shift of its average energy (center of gravity [39, 60]) up to the Fermi energy. This is well illustrated in Fig. 2.6 which shows the d-projected density of states

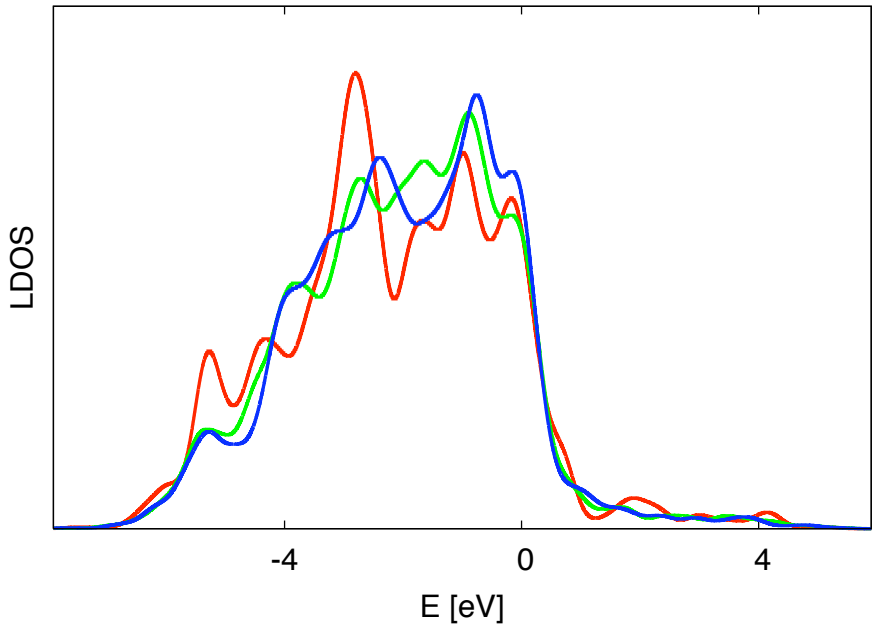

Figure 2.6: Density of states projected on level d for (111) surface atom (red line) and (211) (green line) and (311) step atoms (blue line).

for the three surfaces. Note the similarity between the d-PDOS at steps in (211) and (311) surfaces, whose atoms are equally coordinated. According to the Hammer-Nørskov (HN) model [39, 60], the center of gravity of the d-PDOS of the active metal atom is an indicator of the surface reactivity, in that the less bound the local d band is on the average, the more reactive is the metal atom. In the present case, the center of gravity of the d-PDOS is 2.12, 2.00, and 1.96 eV below the Fermi energy, for atoms at clean surfaces and at (211) and (311) steps, respectively. On the basis of HN model, one should expect therefore an enhanced reactivity going from the flat to the stepped surfaces, as well as a similar reactivity of the steps in the two vicinal surfaces considered in the present thesis. In Figs. 2.7 we display a selection of H, OH, and H_2O adsorption geometries and energies for [211] surfaces. When any of these chemical species is adsorbed on the [111] facets, the adsorption energies do not differ sensitively from the clean [111] surface, whereas the adsorption energy is enhanced at bridge sites on the step ridges. The enhancement is moderate for H and H_2O (from 2.75 to 2.88 and from 0.20 to 0.42 eV, respectively), while it is substantial for OH (from 2.01 to 2.88 eV). Although the precise value of these figures may depend on the details of the density functional being employed, particularly in what concerns the adsorption energy of water, we believe that the qualitative trends can be trusted. In particular, the weak dependence of the hydrogen adsorption energy on the local coordination [59] and the slight enhancement of adsorption of weakly bound molecular species [61] was know from previous studies. We have already observed that water dissociation of Pt surfaces is a late TS reaction. We must therefore expect that the energy of the TS will correlate with that of the products of the reaction (FS) which is dominated by the coordination dependence of the OH adsorption energy. As the latter is much stronger than the adsorption energy of the reactants (water molecules), the reaction barrier results to be substantially lowered by the decreased atomic

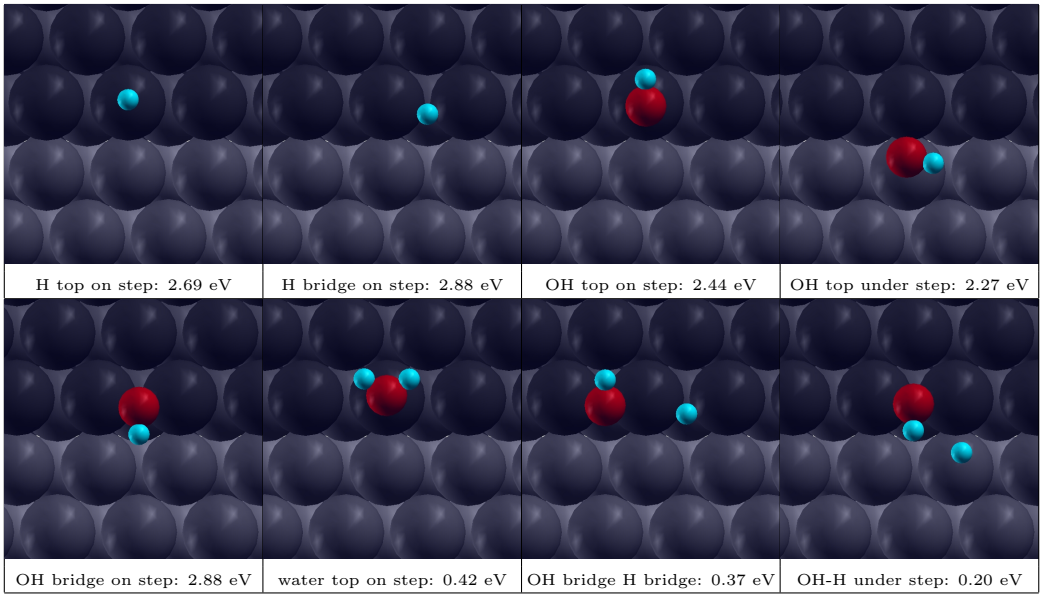

Figure 2.7: Adsorption energies for H, OH, H_2O on 2×1 (211) platinum surface. For H, OH and H_2O reference energy is given from free surface plus free molecule. For products couple (OH + H) reference energy is given by water free molecule plus free surface. Only a selection of data is reported in table.

coordination at the step bridges. This is illustrated in Fig. 2.8 which features a decrease of the reaction barrier (from 0.95 to 0.84 eV), as well as of the energy balance for molecular dissociation (from 0.75 to 0.05 eV).

In Fig. 2.9 we report some of the relevant adsorption geometries and energies at the (311) surface, whereas Fig. 2.10 shows the corresponding initial, transition, and final states of the reaction. The situation is qualitatively similar to that of the (211) surface, the main difference being a slightly smaller adsorption energy for undissociated water in the initial state. This happens because of steric reasons: on Pt(211) the water molecule adsorbs on the ridge of the step with the H atoms bointing towards the (111) facet; on the (311) surface, instead, the (111) terraces are too short and the most convenient

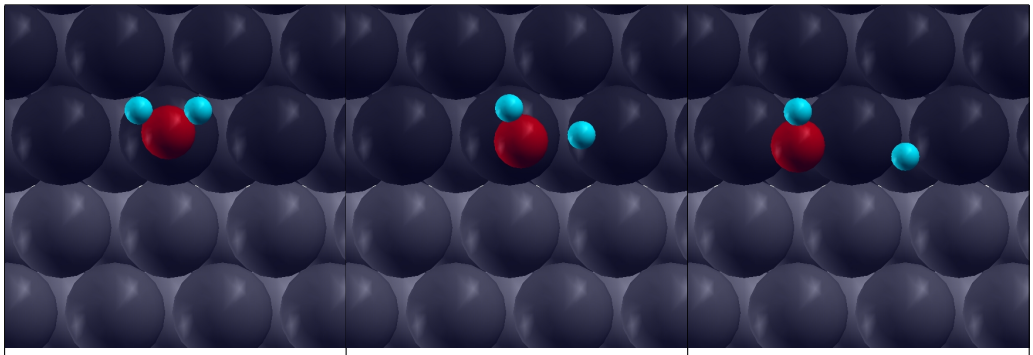

Figure 2.8: Images of initial, transition, and final states for water dissociation on (211) platinum surface. The minimum energy path has been calculated with the NEB technique using 9 images.

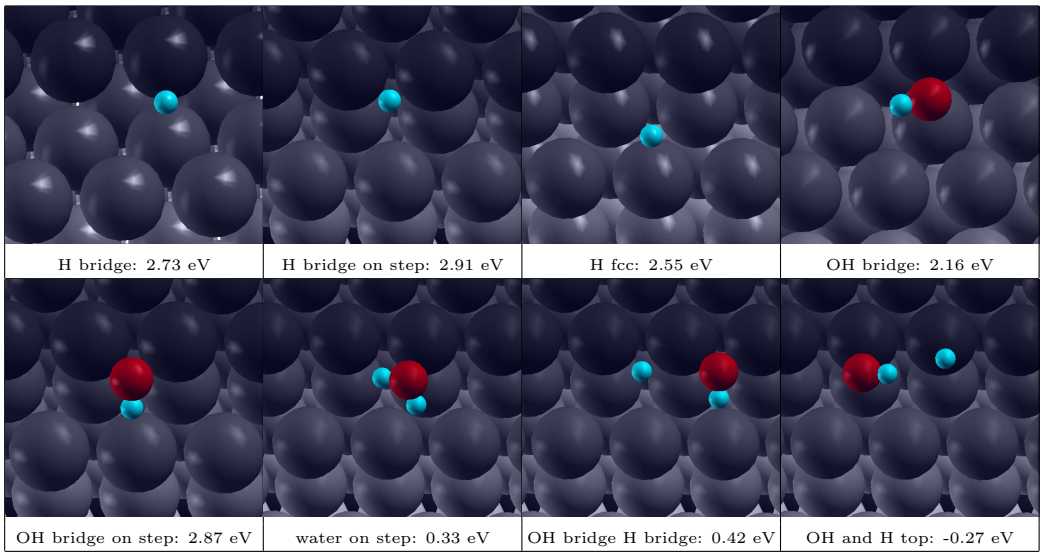

Figure 2.9: Adsorption energies for H, OH, H_2O on $2 \times 1\,(311)$ platinum surface. For H, OH and H_2O reference energy is given from free surface plus free molecule. For products couple (OH + H) reference energy is given by water free molecule plus free surface. Only a selection of data is reported in table.

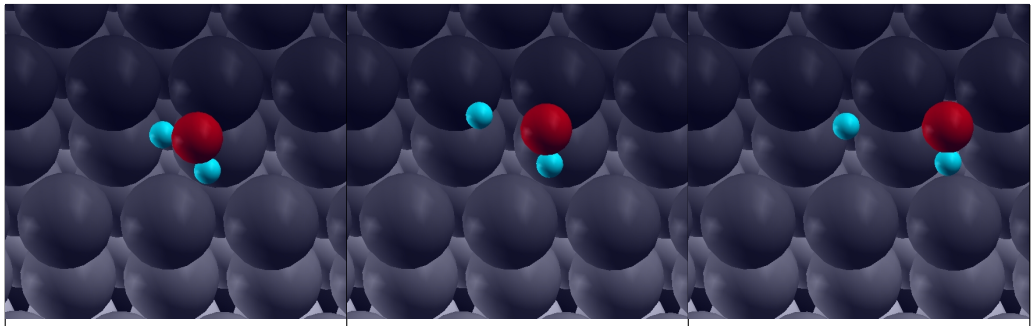

IS: E=0 eV	TS: E=0.72 eV	FS: E=-0.09 eV

Figure 2.10: Images of initial, transition and final states for water dissociation on (311) platinum surface. The minimum energy path has been calculated with the NEB technique using 9 images.

orientation of the water molecule has the H atoms pointing towards a (100) facet underneath. As a result, the barrier for the forward reaction, as well as the energy balance for dissociation results to be lowered by about 120 and 140 meV respectively, whereas the barrier for the inverse (recombination) reaction remains substantially unchanged from (211). In Table 2.1 we summarize the main results of the present calculations. We notice that the increased reactivity of the surface steps on Pt(111) results in a dramatic increase of the adsorption energies of the products of water dissociation, as well as in the decrease of TS energies, which turn out to be substantially equal in Pt(211) and Pt(311). These facts correlate nicely with observed behavior of the center of gravity of the metal d band, also reported in Table 2.1. The difference between the activation energies for water dissociation in Pt(211) and Pt(311) are due to a large extent to the different adsorption energies of the undissociated molecule in the initial state, as previously discussed.

	E IS	E TS	E FS	Center of d-PDOS
Pt(111)	-200	750	560	2120
Pt(211)	-420	420	-370	2000
Pt(311)	-330	390	-420	1960

Table 2.1: Energies in meV of the initial (IS), transitions (TS) and final states (FS) for water dissociation in various Pt surfaces. The last column reports the calculated center of gravity of the electron density of states projected on the d orbitals of the metal reaction center (meV).

2.4 Conclusions

The results presented indicate that the dissociation of water on Pt(111) surfaces is facilitated by the presence of steps, due to the enhanced reactivity of atoms with a lower coordination. Water dissociation is a late transition state reaction, where the reactant is weakly bound to the surface and the products are almost dissociated already at the transition state. Therefore, the binding of the H+OH products is much more enhanced by the reduced coordination than the binding of the reactant molecule. As a result, while the dissociation is strongly endothermic on the flat surface ($\Delta E \sim +0.75$ eV), it is much less so, or even exothermic, on stepped surfaces ($\Delta E \sim +0.05$ and ~ -0.09 eV for the (211) and (311) surfaces, respectively). The activation energy for dissociation varies accordingly, but not as pronouncedly: $\Delta E^* \sim 0.95, 0.84$, and 0.72 eV for the (111), (211), and (311) surfaces, respectively). As a consequence of the more pronounced dependence of the energy of the final state on atomic coordination than than of the transition state, water formation is instead hindered at steps (the corresponding calculated barrier varies from $\Delta E^* \sim 0.19$ in Pt(111) to 0.79 and 0.81 eV at the steps of Pt(211) and Pt(311)).

Chapter 3

Hydrogen and oxygen on rhodium (111)

The study presented in this chapter has been motivated by a collaboration with an experimental group at ELETTRA Synchrotron Light Source laboratory. It regards the kinetics of water formation on Rh(111) from reactants (H_2 and O_2) in the gas phase. The ability of transition metal surfaces to activate the $H_2+\frac{1}{2}O_2 \rightarrow H_2O$ reaction is known to have a strong dependence on the surface coverage of the different adspecies, which dramatically varies by changing crystal composition and orientation. For Ru(0001), for example, the reaction rate vanishes when approaching a critical low oxygen coverage. This is explained by the structure sensitivity of the reaction rate: at $\theta_O = 0.25$ ML an unreactive p(2×2) superstructure is formed, while at sligthly higher oxygen coverage a transformation into much more reactive domains occurs [62]. On the contrary, on Rh(111) for oxygen coverage below a critical value, the exposure of the surface to H_2 leads to the immediate evolution to H_2O, while for a larger O population ($\theta_O \approx 0.5$ ML) the water evolution is not as rapid; there is an induction period wherein the rate of H_2O production growth, before rapidly falling as soon as the O is depleted [19]. This behavior

is expected if the reaction is not structural sensitive and if it proceeds by a Langmuir-Hinselwood mechanism [63], in which both reactants adsorb before reacting. The first reaction step is the dissociative adsorption of molecular hydrogen and the dissociative sticking coefficient is much higher on the bare Rh surface than on an oxygen overlayer. As the quantity of O increases, the number of vacant Rh sites for H_2 dissociation decreses and the reactivity lowers accordingly. However, not much is known about the particular reaction mechanism between chemisorbed H and O on Rh(111) and the corresponding activation energies to form water in these conditions. Although a simple reaction mechanism might be expected, as only two different atomic species are involved, several reaction regimes can be present depending on pressure and temperature. This could include the developement of reaction fronts, the autocatalytic behavior of the reaction or the peculiar contribution of complex lateral interactions between the surface species. Indeed, recent experiments based on High Energy Resolution Core Level Spectroscopy performed at the SuperESCA beamline of ELETTRA have shown that reactions occurring on the surface are only compatible with the removal of couples of neighboring oxygen atoms at high oxygen coverage ($\theta_O = 0.5$ ML), while at lower coverage ($\theta_O = 0.25$ ML) water formation rate is consistently higher.

Stimulated by these experiments, in this chapter we are going to explore by means of DFT the kinetics of hydrogen and oxygen reaction on Rh(111). In the next section we will present and discuss the experimental setup and results. In the second and third sections we'll discuss our calculations for the stability of various chemical species on Rh(111). In the last section we'll present results for energy barrier calculations for reactions between chemisorbed hydrogen and oxygen, paying also attention to the possibility that hydrogen peroxide is produced on the surface.

3.1 Experimental data

Calculations presented in the following have been motivated by a time-resolved high-resolution X-ray photoemission experiment performed at the ELETTRA Synchrotron Light Source laboratory by Alessandro Baraldi and collaborators. Spectra obtained with this technique give informations on electronic core level structure that univocally identify the emitting element. Small variations of the core levels of a same element on the scale of a fraction of an eV are sensitive to the local chemical environment of individual atoms (Core Level Shifts).

With this very refined set of tools it is possible [64] to identify on an oxygen covered Rh(111) which rhodium atoms in the first layer are bonded to oxygen and the coordination number of each one. Thanks to the high energy resolution and high photon flux of synchrotron radiation in the soft X-rays, we can monitor populations of differently coordinated rhodium atoms *in-situ* during a chemical reaction, with the adeguate time resolution. These data are useful to understand the kinetics of the reactions occurring on the surface. An example of the results we can obtain is presented in figure 3.1, in which we have shown a time-resolved set of spectra for a Rh(111) gradually exposed to an oxygen atmosphere.

Depending on experimental conditions (pressure, temperature and time of exposure) oxygen on metals can have different behaviors. The most frequent result is the dissociative adsorption of oxygen, but if conditions are varied we can obtain the formation of subsurface oxygen or surface oxidation. Density functional calculations predict that very high-coverage adsorbate layers are possible (1 ML) to the point where it is not easy to classify the structure as adsorption or oxidation. Experimentally it is typical to observe 0.5 ML coverage on rhodium (111) surface starting from molecular oxygen because, once we have reached this coverage, oxygen dissociation probability drasti-

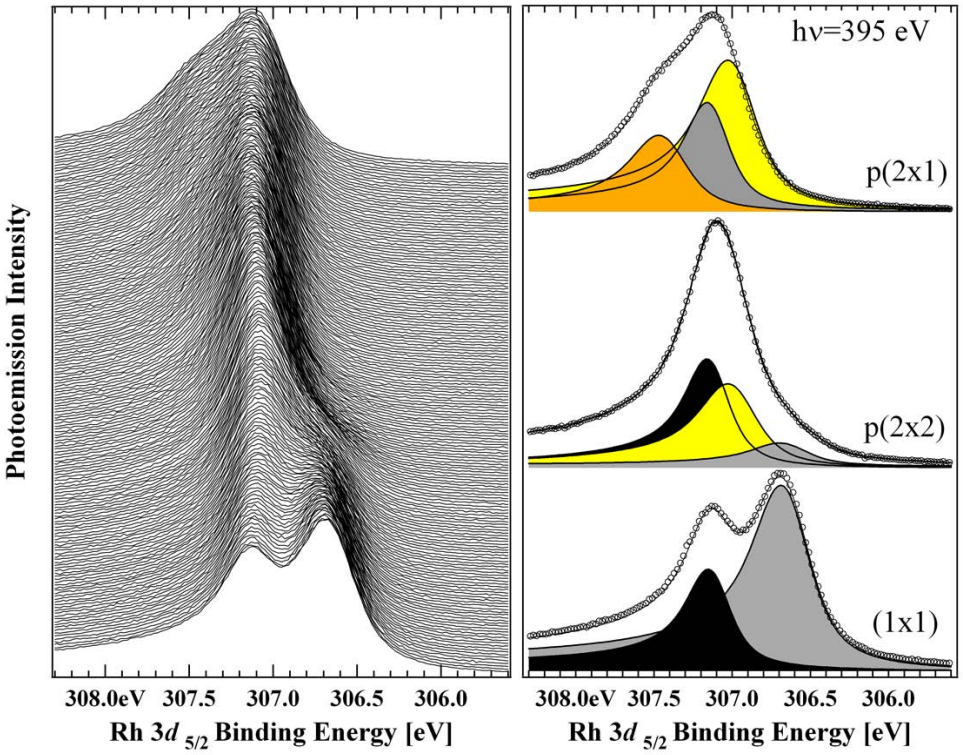

Figure 3.1: Example of Surface Core Level Shift experimental data of a Rh(111) surface in oxygen atmosphere. Accuracy declared is 20 meV. Comparison of the spectra obtained for three surface structures corresponding (from bottom to top) to an oxygen coverage of 0 ML, 0.25 ML and 0.50 ML. In the left the time evolution shows the formation, starting from a clean structure, of a p(2×1) $\theta_O = 0.5$ ML. Spectra are decomposed in components: black is bulk, grey is uncoordinated surface atom, yellow and red are respectively once and twice coordinated to oxygen atoms.

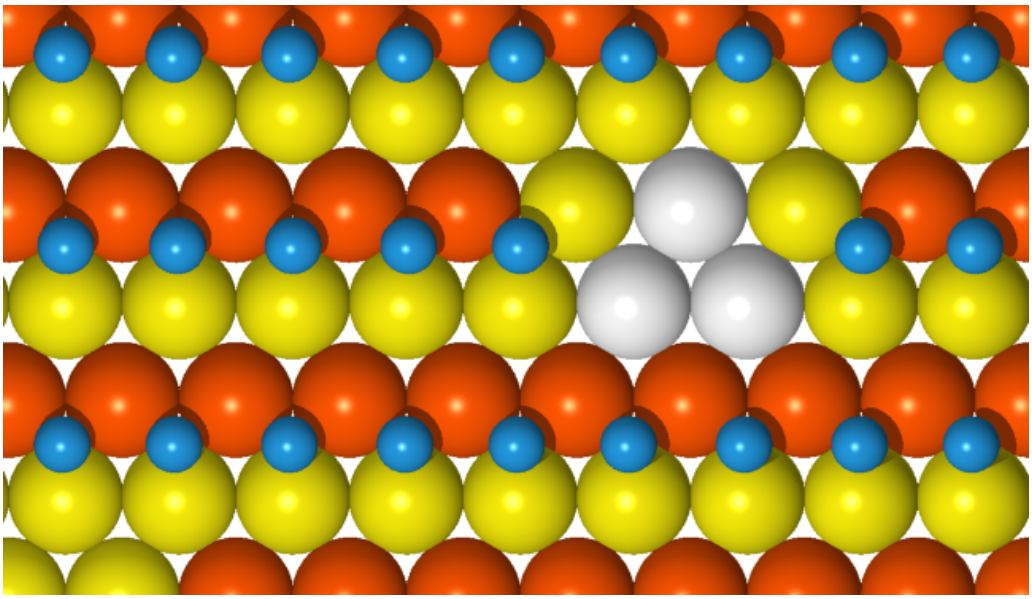

Figure 3.2: The colors enhance the coordination of the first layer rhodium atoms. Red corresponds to double coordinated Rh, yellow to single coordinated and grey to uncoordinated to any oxygen atom.

cally diminishes. It has been recently pointed out in some experiments that for high temperature and large exposure we can obtain an overall coverage intermediate between 0.5 ML and 1.0 ML, caused by formation of zones with 0.5 ML and zones with 1.0 ML sparse disorderly on surface [64].

In the conditions of the experiment performed at ELETTRA, the maximum measured coverage is 0.5 ML. This configuration, as we have verified with DFT calculations, corresponds to p(2×1) ordered layer of oxygen atoms in threefold position (fcc is preferred to hcp). In an ordered 0.5 ML structure, as the one pictured in figure 3.2, we see alternate rows of twice coordinated atoms (we'll draw them in red/orange color and we'll call them "red") and once coordinated atoms (we'll draw and call them "yellow"). If we have some vacancies, we can also zero coordinated atoms (coloured and called "grey").

The picture 3.3 summarizes the experimental results we want to discuss.

The rhodium (111) surface has been kept to a temperature of 520 K. The lasting time of all the process is 600 seconds, a constant hydrogen pressure of 10^{-8} mbar has been kept to ensure abundance of hydrogen adsorbates on surface (we can easily assume that an hydrogen atom is always near and ready to react) while oxygen pressure was modulated between 0 and 2×10^{-7} mbar by using a supersonic molecular beam. It has been tracked population (in fractions of the unity) of grey, yellow and red atoms, the sum of all the three (1 by definition) together with the oxygen coverage. The water production rate was monitored in parallel by means of a mass spectrometer.

The first thing that we notice (figure 3.3) is that the system does not reach precisely 0.5 ML that should lead to 0.5 red atoms and 0.5 yellow. This is easy to understand, given the presence of reactions involving hydrogen. The main interesting behavior is given by the correlation of yellow and red populations. In a random picture in which everywhere fast water production occurs, we expect an initial decrease of the red population versus yellow grows. If an oxygen is removed in an uniform 0.5 ML we should have a couple of red turning into yellow and a yellow coming grey, leading to an overall result of two reds coming into a yellow and grey. On the contrary the experimental results show that the yellow population is constant while red is going all into grey: this is compatible only with a removal of a couple of neighboring oxygen atoms. Once the red is no more populated, the yellow decrease is fast and this corresponds to a large water production, evidence of the presence of very fast reactions on the surface between chemisorbed oxygen and hydrogen.

We want justify these results through the energy barriers computed for the different possible processes. In the perspective of the research for a hydrogen peroxide catalyst two interpretations are promising. We could have found a regime (High oxygen coverage) in which water formation is slow (principal concurrent to peroxide formation). The simultaneous removal of a couple of near oxygen atoms could be compatible with the direct formation of a

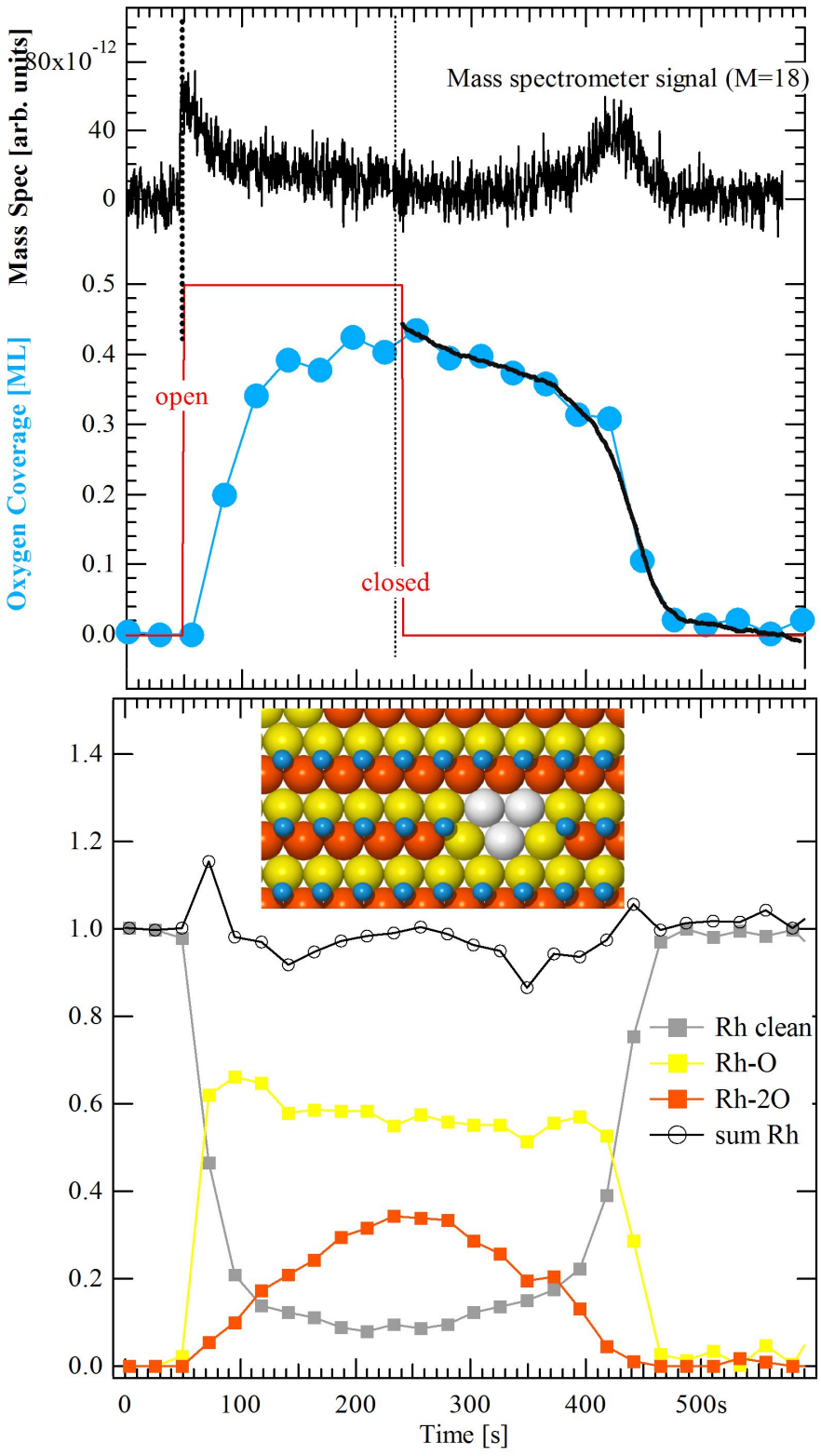

Figure 3.3: Rh(111) exposed to oxygen in an hydrogen atmosphere. Populations of differently coordinated surface rhodium atoms is measured through SCLS. The correlated water formation rate is obtained through mass spectrometry.

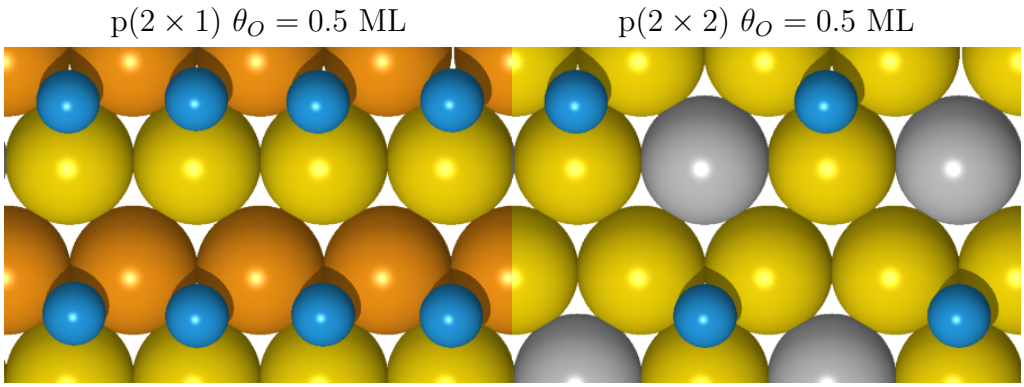

Figure 3.4: An homogeneous removal of half of the oxygen coverage from the surface, with large production of water should lead to fast removal of "red" rhodium atoms, with a corresponding increase of "yellow" population, not spotted in the experiment.

hydrogen peroxide molecule, not recognized by our mass spectrometer that is tuned to mass 18 (hydrogen peroxide is very difficult to spot in this kind of measures).

Finally we have to answer to many questions:

1. what reactions are compatible with the removal of a couple of near oxygen atoms;
2. how large is water formation barrier in this regime;
3. if some concurrent process is present in this regime, is it compatible with hydrogen peroxide formation?

3.2 Rhodium (111)

Rhodium is a cubic closed packed (fcc) solid with 0.380 nm cell dimension [53] and 275 GPa bulk modulus from experimental data [65]. Our calculations

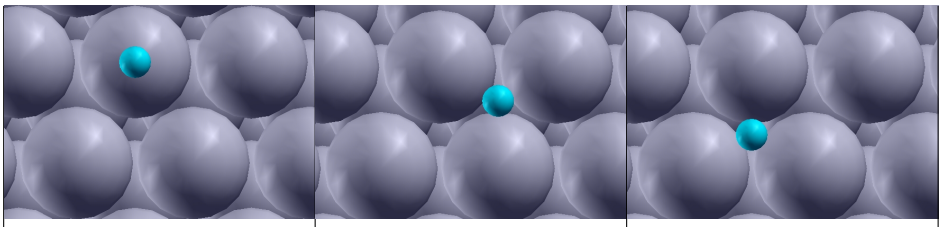

top: 2.51 eV	hcp: 2.81 eV	fcc: 2.82 eV

Figure 3.5: Energy gain for hydrogen adsorption at symmetry points of Rh(111) p(2×2) from our DFT calculations. Bridge position is unstable.

predict 0.387 nm cell dimension and 286 GPa bulk modulus. We have used ultrasoft pseudopotentials with GGA DFT. To ensure millirydberg consistency in calculations we have used a 30 Ry cutoff for wave functions, 200 Ry cutoff for density, and 10 mRy smearing with Methfessel-Paxton first-order spreading [66]. The k-point grid for bulk was a $8 \times 8 \times 8$ Monkhorst-Pack grid displaced by half a grid step in the each direction. For 2×2 (111) surface calculation this grid was reduced to $4 \times 4 \times 1$ and consistently to $4 \times 2 \times 1$ for 4×2 supercell and $2 \times 2 \times 1$ for 4×4 supercell.

Techniques are very similar to ones used in platinum calculations. Since during calculations described in previous chapter we have realized that our choice of 4 slabs relaxing with one fixed was very prudent (differences between 4 with one relaxing and 3 with all fixed are negligible in adsorption energies and barriers), and since the computational effort is larger for the kind of system we are going to investigate, we have switched to a different model of our surface. In fact we have performed fast calculations, using 3 slabs of the 111 surface, where the first is allowed to relax.

Moreover, even if we have realized that the minimum super-cell suitable to describe conditions similar to experiment is at least 4×4, first calculations have been performed on 2×2 cell. Only in a second moment we have switched to 4×2 supercell and finally a selection has been compared with accurate

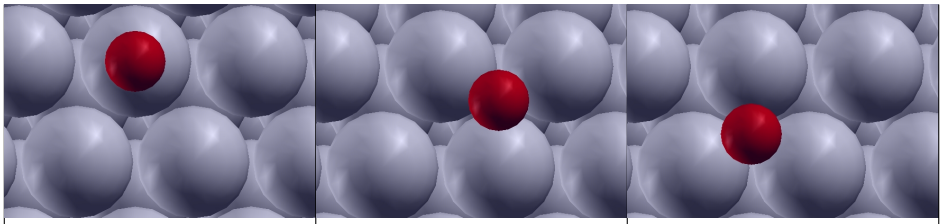

top: 3.78 eV	hcp: 5.03 eV	fcc: 5.08 eV

Figure 3.6: Energy gain for oxygen adsorption at symmetry points of Rh(111) p(2×2) from our DFT calculations. Bridge position is unstable.

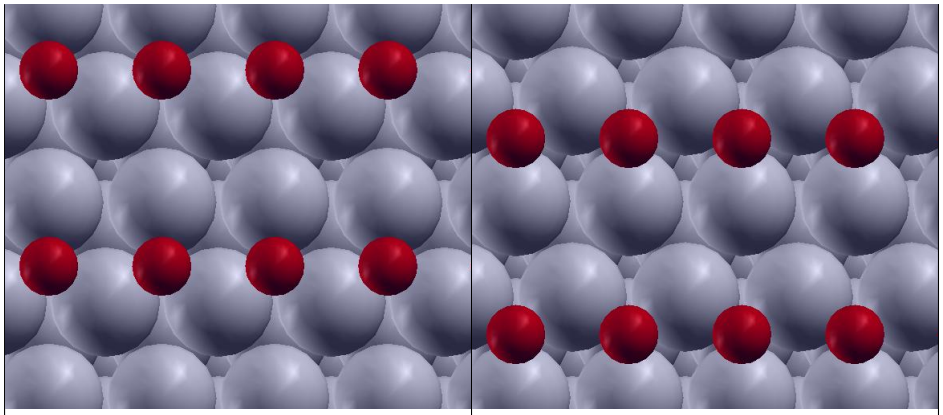

fcc: 4.24 eV	hcp: 4.08 eV

Figure 3.7: Energy gain for a couple of oxygen atoms adsorbed at $\theta_O = 0.5$ ML p(2×1) from our DFT calculations. Reference is oxygen molecule in the vacuum.

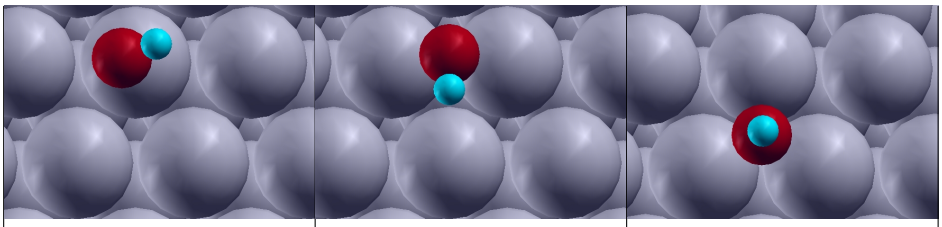

top: 2.78 eV	bridge: 3.03 eV	fcc: 3.01 eV

Figure 3.8: Energy gain for hydroxyl adsorption at symmetry points of Rh(111) p(2×2) from our DFT calculations. Hcp position is unstable versus bridge.

4×4 supercell calculations.

Adsorption energies for H, OH and O at 0.25 ML coverage have been calculated. Dario Alfè [67] has provided us initial tips and reference about these species on the same system. After his suggestions we have chosen a suitable pseudopotential[1] in the library avaible on line [52, 68]. He has verified that 0.25 ML is sufficient to describe with a good accuracy adsorption energies at low coverage. Moreover we have reproduced most of his results for comparison (figures 3.5, 3.6 and 3.8). Diffusion energy for H from a NEB calculation with 9 images on a Rh(111) p(2×2) is 90 meV, while for OH is 240 meV. The p(2×1) structure with oxygen on fcc site, that describe initial conditions of the experiment, has been reproduced (fig. 3.7).

3.3 Hydrogen peroxide

The most used process to produce hydrogen peroxide at industrial levels is actually the standard anthraquinone process [69, 70] which is expensive and generates pollution (anthraquinone is a bird repellent pesticide; its formula

[1]The one chosen for rhodium has non linear core corrections and d states in valence band.

rOH	0.950	0.982
rOO	1.475	1.472
aHOO	94.8	99.81
dHOOH	119.8	114.31

Table 3.1: Experimental data [72] and our DFT calculations. Distances are in angstrom, angles in degrees, d is dihedral angle.

is $C_{14}H_8O_2$). Moreover it can oxide and be poisoned for the reaction.

Catalysts which involve palladium in liquid phase are used since 1914 [71] but there are open issues:

1. to ensure selectivity among water formation in such a way to produce the purest hydrogen peroxide;

2. to avoid explosions due to fast reaction between H_2 and O_2 to form water.

Point 1 can be achieved if the metal surface is hydrorepellent, for example if the first layer is oxidized or if the substrate is covered by hydrorepellent substances. Rhodium (111) is not the best suitable surface because it is an efficient water producer. By the way we can imagine that its properties are modified by oxygen coverage as we'll show later. To achieve point 2 there are experiments about membrane triphasic catalysts. Catalyst is palladium in acidic solution [21, 22, 20, 23].

Moved by the charming hypothesis about experimental data regarding hydrogen peroxide formation, a first part of our calculations has been focused on the study of this molecule properties. In figure 3.9 we see the comparison between two different geometric structure of hydrogen peroxide obtained with *ab-initio* calculations. In the table 3.1 we can compare experimental data with our DFT calculations. Not all the basis sets are suitable to correctly

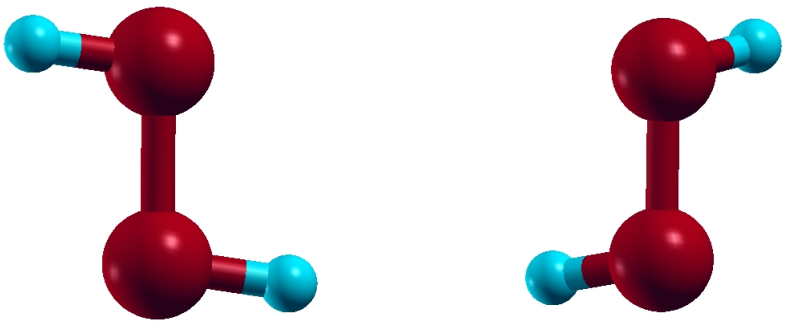

Figure 3.9: 3D images of H_2O_2 from our DFT calculations. First one has a planar structure, while the second one a realistic structure

reproduce hydrogen peroxide geometry. Calculations are sensitive to the choice of basis and can give as result a not realistic planar geometry [72] for H_2O_2 so that usually the basis is extended to 6-31G* to obtain a good agreement. Our plane wave calculations with ultrasoft pseudopotential and PBE GGA functional give good result for the geometry if energy cut off for plane waves is chosen to be at least 30 Rydbergs. The planar structure of H_2O_2 calculated is only 50 meV higher in energy.

Hydrogen peroxide is unstable versus dissociation into water and oxygen. Experimental barrier for the reaction

$$H_2O_2(l) \rightarrow H_2O(l) + 1/2O_2(g) \tag{3.1}$$

is 1.01 eV [73]. With a NEB calculation of a similar reaction (molecules in a box and so gas phases) we have obtained 1.05 eV. A NEB calculation for the reaction

$$H_2O_2 + H_2 \rightarrow 2H_2O \tag{3.2}$$

has been performed with the same conditions and gives 1.80 eV.

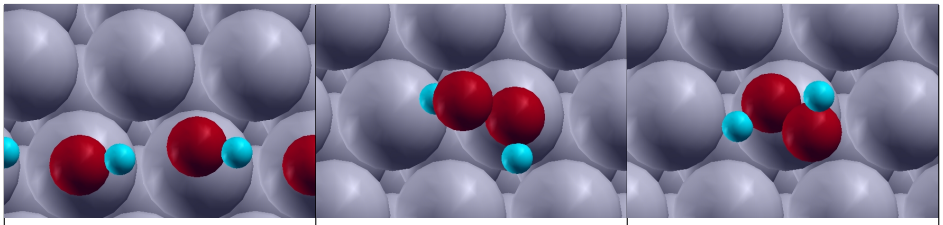

Dissociated: -2.93 eV	Best: -0.41 eV	OH planar: -0.34 eV

Figure 3.10: Some examples of results for hydrogen peroxide relaxations on rhodium (111). It was not simple to find some stable positions because the molecule is unstable versus the dissociation into a couple of hydroxyls.

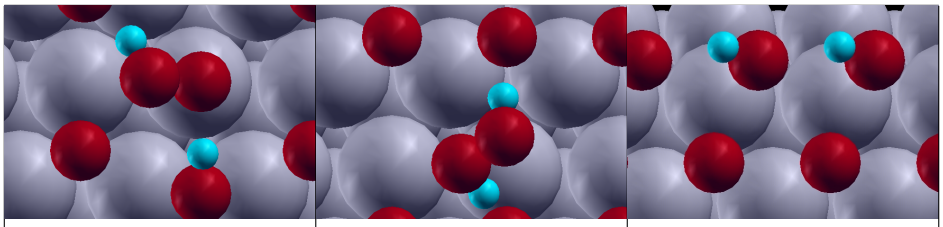

OOH and OH: -0.63 eV	H_2O_2: -0.14 eV	2 OH: -0.86 eV

Figure 3.11: Similar to figure 3.10 but on a 0.5 ML oxygen covered rhodium (111). 2×2 supercell calculations

On metallic surfaces hydrogen peroxide is much more unstable versus decomposition. In fact it has not been easy to find hydrogen peroxide species bound to Rh(111), because many structure optimizations resulted in a couple of bound hydroxyls with an huge energy gain (about 2.5 eV). In figures 3.10 and 3.11 we give a summary of energetic study of hydrogen peroxide on Rh(111). On the clean surface it is very difficult to obtain from relaxation an undissociated hydrogen peroxide molecule, while on an half oxygen covered surface it is easier. Even if adsorption energy is negligible, dissociated species have lower gain in energy compared to the clean Rh(111).

3.4 Hydrogen on oxygen covered Rh(111) surface

Following the scheme in picture 3.2 we are going to investigate reactions that can lead to the simultaneous or at least the fast removal of a couple of near oxygen atoms from the surface. In fact evidences from experiments, as we have early commented, suggest that when the coverage is high (near 0.5 ML) only couple of near oxygen atoms from the same line disappear, causing a lowering in the double coordinated rhodium atoms and an increasing of zero coordinated atoms. Let's remember that we will call "red" the double coordinated atoms, "grey" the zero coordinated atoms and "yellow" the one coordinated atom.

Using the same NEB technique applied to platinum surfaces calculations, we have calculated several barriers to explore possible reaction paths. A very charming hypothesis about the simultaneous removal of a couple of oxygens from the surfaces brings to the idea of rhodium surface activating catalytic formation of hydrogen peroxide. As we have discussed earlier, hydrogen peroxide formation can be favoured by hydrorepellent surfaces. Rhodium is not hydrorepellent and in fact a molecule of hydrogen peroxide fast breaks into two hydroxyls with a consistent gain in energy. By the way, if the surface is perfectly half covered of oxygen neither water binds on it nor hydrogen peroxide reacts breaking. Our configuration with such a high coverage of oxygen is not in contrast with this picture, but inspection of figure 3.11 shows that a couple of hydroxyls should be formed at first and soon penetrate the rows of oxygen atoms. Activation energies for diffusion of the species involved need to be estimated and considered. Other more exotic paths can lead to intermediates like HOO radical (not energetically far) or O-H-O moiety (very unstable configuration, about 10.5 eV higher).

First step for each reaction is the formation of an OH. So this is the

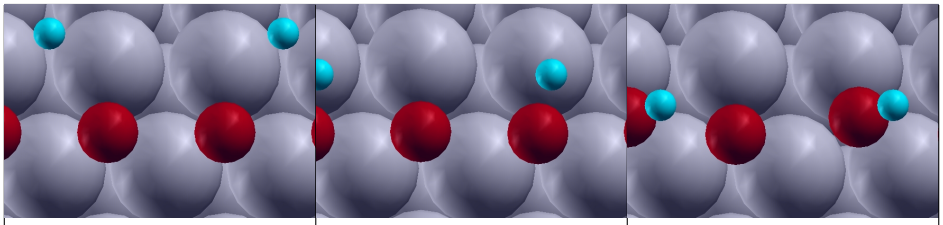

Figure 3.12: Formation of first OH on a p(2×1) oxygen covered Rh(111). NEB calculations with 9 images on a 2×2 supercell.

first limiting barrier to be computed. Molecular hydrogen easily breaks and diffuse on Rh(111) surface so we can consider it, in the conditions of our experiment, present on the surface. It prefers in our configurations to occupy hcp positions while fcc ones are taken by oxygen atoms.

3.4.1 DFT calculations

In the preliminary calculations we have performed, with the same 2×2 cell used by Dario Alfè [67], we have investigated four processes:

1. formation of first OH (fig. 3.12): energy barrier of 0.94 eV;
2. formation of second OH (fig. 3.13): energy barrier of 0.89 eV;
3. simultaneous formation of two OH (fig. 3.14): energy barrier of 0.98 eV;
4. water formation after first OH (fig. 3.15): energy barrier of 0.25 eV.

In the picture of hydrogen peroxide formation, we should expect low values for barriers of the reactions depicted in figures 3.13 and 3.14 compared to the 0.94 eV barrier for formation of first OH. These preliminary calculations are not consistent with this model and it is clear that in this regime

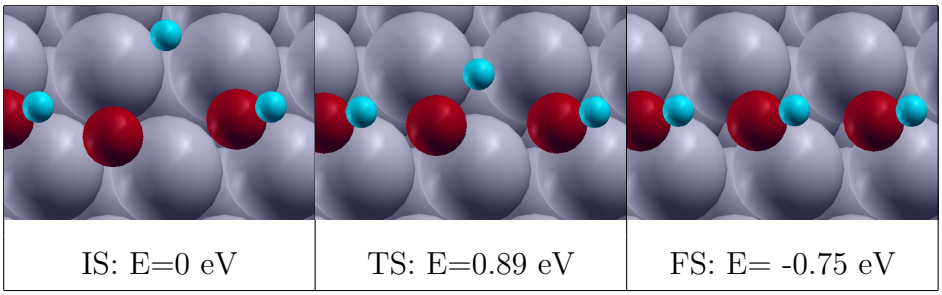

Figure 3.13: Formation of second OH, after the first reaction described in picture 3.12, in a 2×2 super-cell. NEB calculation with 9 images. As we can see from the third column a 2×2 super-cell is not adeguate to correctly describe our system.

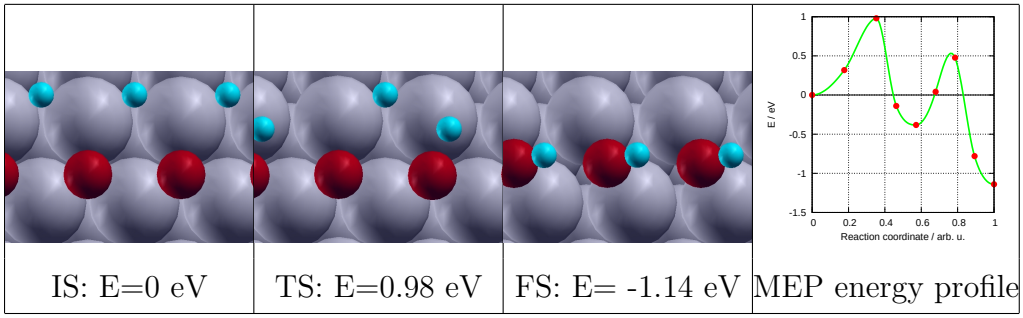

Figure 3.14: Simultaneous formation of 2 OH in a 2×2 super-cell. In the fourth column we can see the energy profile of the nine images of our MEP. As we can see from the third column a 2×2 super-cell is not adeguate to correctly describe our system. It is very interesting to notice that the path is nearly a first OH formation followed by a second one that is lower in energy barrier. This has to be compared with the path in figure 3.13 and gives us an hope than under appropriate conditions the formation of second OH is effectively lower in energy barrier.

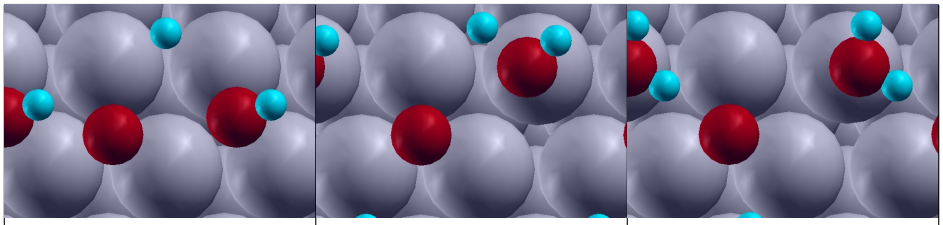

Figure 3.15: Formation of water in a 2×2 super-cell. NEB calculation with 9 images.

water formation is the preferred route. We have to notice that, reducing our super-cell to a 2×2 creates some artifacts, due to interactions between periodic images of molecules. The final state is also not properly described because a whole row of OH is formed because of periodic replica. By the way we obtain useful indications for successive and more expensive calculations.

Immediate formation of a second OH near the first on the same line is not the process we are looking for, because it is compatible not only with a removal of a couple of oxygens, but also with a front-line reaction. We should check in fact the third OH formation barrier to be sure that after the first two steps, reactions should not proceed with induction on the entire row.

Moving to a larger 4x2 cell we have computed diffusion barriers for H atom and OH after formation. Hydrogen diffusion has been computed about 0.25 eV in a direction perpendicular to the oxygen row and 0.30 eV to penetrate a double row. These barriers are of the same order of water formation barrier and since transition state depicted in figure 3.15 is a late transition state we could expect that hydrogen diffusion is the limiting process. Mobility of hydrogen in this regime is lower compared to low coverage oxygen (clean surface hydrogen diffusion barrier is much lower in our DFT calculations: 90 meV). OH, starting from the position where it is formed, can diffuse perpendicularly to the row with a computed barrier of 40 meV (al-

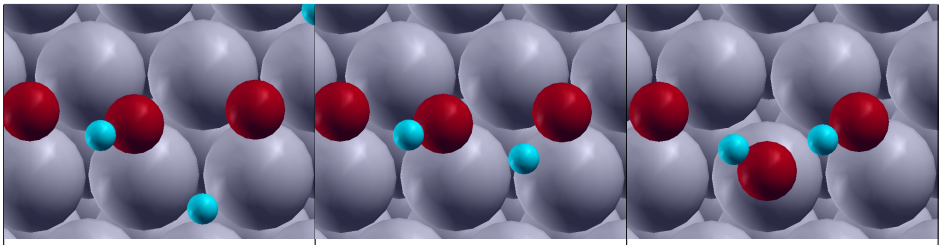

Figure 3.16: Moving to a more precise 4×2 super-cell does not decrease energy barrier for formation of a second OH in this configuration.

most barrierless), 150 meV are necessary to run between lines and 380 meV to penetrate the lines from outside (figures 3.17 and 3.18).

In figure 3.19 we show an evidence that, after a negligible barrier diffusion of OH, routes for a formation of a second OH are possible. The barrier for the process depicted is just 260 meV, comparable with direct water formation. An intermediate state is similar to a water molecule, in a sort of autocatalytic process. Indeed, autocatalysis for the reaction $H_2O+O \rightarrow$ 2 OH, after water formation, calculated on 4×2 supercell is resulted higher in barrier (550 meV) for the simple fact that water molecule is lower in energy than the couple of hydroxyls.

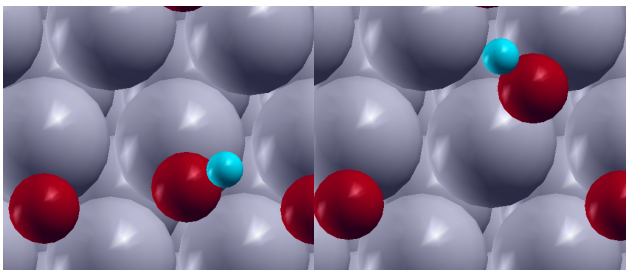

Figure 3.17: Simple movements of OH from its generating point towards a direction perpendicular to the O rows are mostly barrier-less. For simmetry reasons this is the same for little movements (without penetrating a double row) in the perpendicular direction. 2×2 super-cell calculations. 40 meV is the computed barrier value.

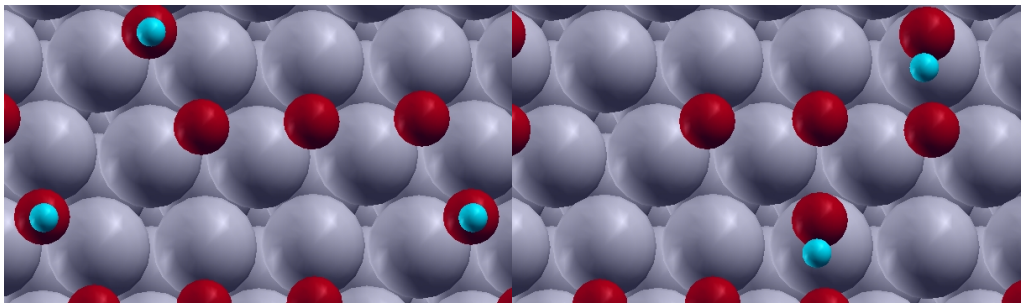

Figure 3.18: OH can diffuse and run along lines. Running costs about 150 meV since we can imagine that moving just passes through slightly similar configurations. Instead it needs to break up a 380 meV barrier to get into a row from outside. To activate process in figure 3.19 it is not necessary to penetrate completely in the double row.

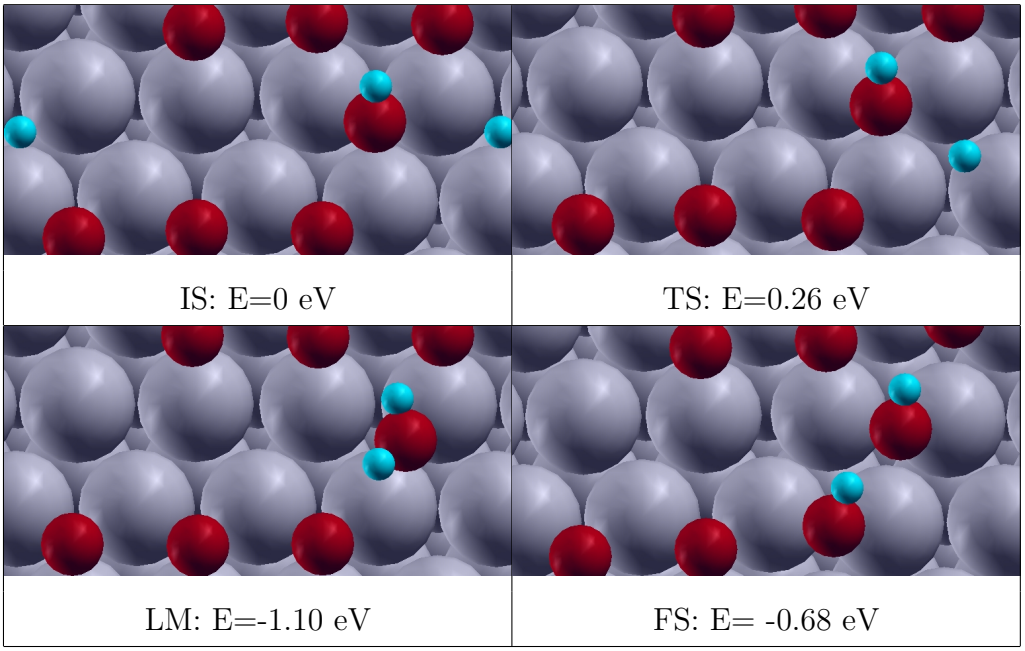

Figure 3.19: The first strong evidence that a fast route to formation of a second OH concurrent to direct formation of water is possible. We sketch an intermediate state that is similar to a water molecule. We see in this pictures the three main states and the local minimum (LM). NEB calculation with 15 images on a 4×2 supercell.

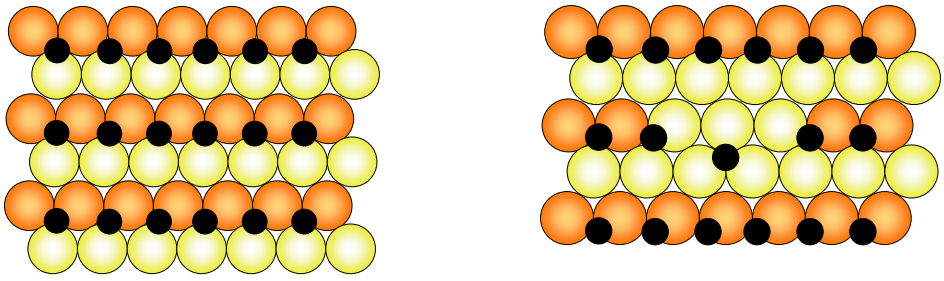

Figure 3.20: A top view of a rhodium (111) surface with 0.5 ML coverage of oxygen atoms. After a water has been formed and removed from the surface, an oxygen atom prefers to move to a different site.

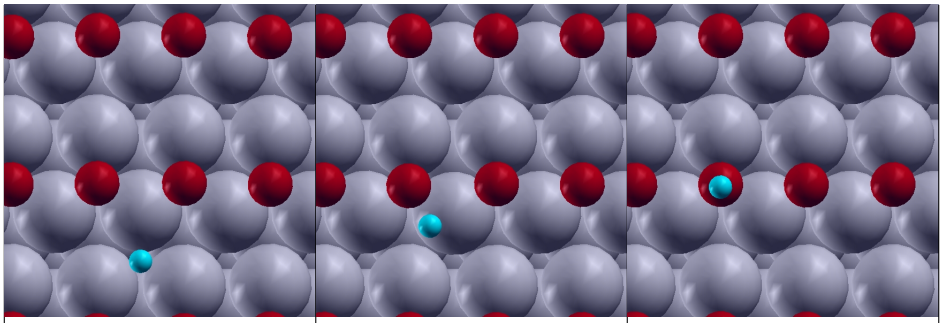

Figure 3.21: Barrier for formation of first OH in the definitive supercell 4×4 from NEB calculations with 15 images to be compared with figure 3.12.

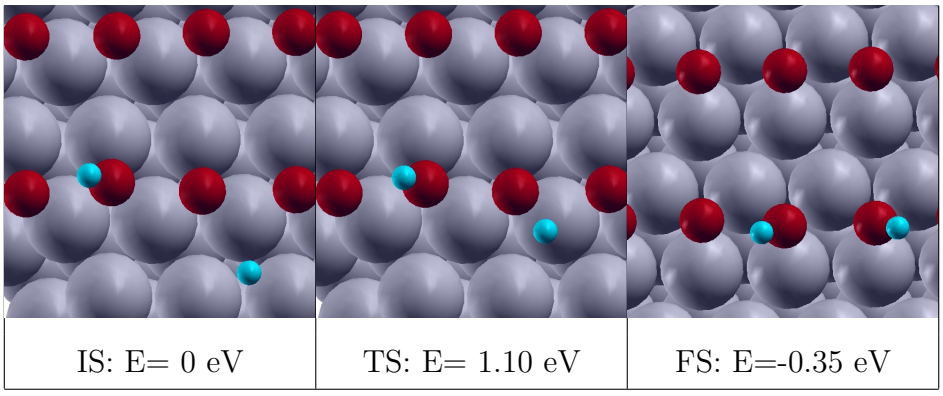

Figure 3.22: This path for formation of a second OH gives no differences compared to figure 3.21. We suppose that the first OH should take an active role in the reaction, but in this path it is a dumb spectator. NEB calculation with 15 images on a 4×4 supercell.

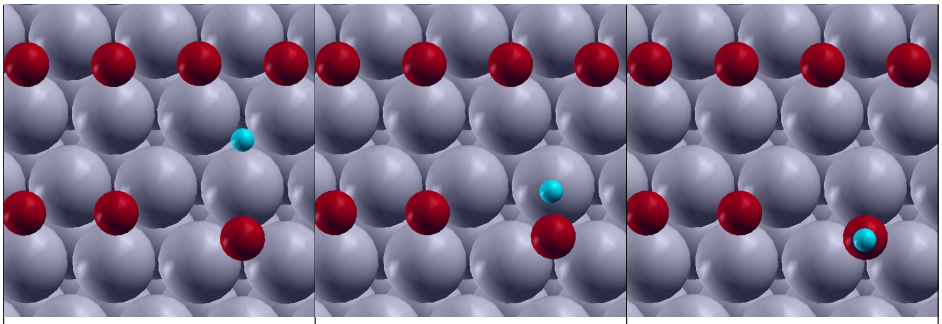

Figure 3.23: Diffusion of an O, after a first water removal does not change significantly the energy barrier for OH formation. NEB calculation with 15 images on a 4×4 supercell.

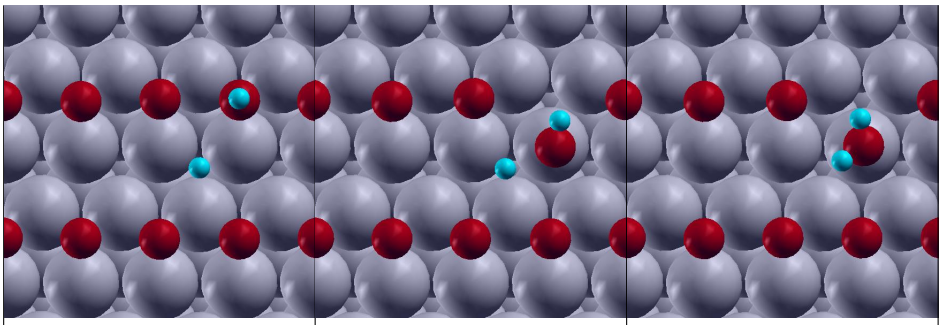

Figure 3.24: Water formation after first OH formation. NEB calculation with 15 images on a 4×4 supercell.

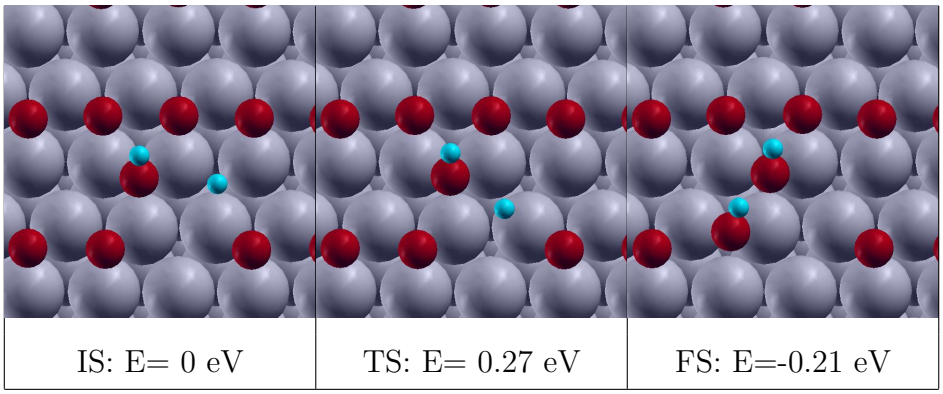

Figure 3.25: Second OH formation after almost barrierless first OH diffusion. NEB calculation with 15 images on a 4×4 supercell.

Last calculations have been performed on the definitive 4×4 supercell. This configuration permits to explore another route for reaction as we can see in figure 3.20. After direct water formation from first OH, it could easily desorb and oxygen atoms rearrange to a more favorable position. We can assume that for the isolated oxygen atom in hcp position OH formation barrier is lower. In this picture the final explanation should be a fast second water formation after the first is gone.

Our definitive and most accurate NEB calculations with 15 images on a 4×4 super-cell contradict this hypothesis:

1. formation of first OH (fig. 3.21): energy barrier of 1.09 meV;

2. formation of second OH (fig. 3.22): barrier of 1.09 meV;

3. formation of OH (fig. 3.23) from O in hcp: 1.04 meV;

4. formation of water (fig. 3.24): barrier of 0.20 meV;

5. formation of second OH (fig. 3.25) after first OH diffusion: 0.27 meV.

3.5 Conclusions

The experiment performed at the SuperESCA beamline of ELETTRA with the High-Energy Resolution Core level Spectroscopy allowed us to monitor dynamics of atomic oxygen on a Rh(111) surface in a hydrogen atmosphere. It is clear from the experimental data that there are two different regimes for reactions between adsorbed oxygen and hydrogen, corresponding to a p(2×1) and a p(2×2) structures, caused respectively by a 0.50 ML and 0.25 ML oxygen coverage. The experimental intensity behavior of the differently coordinated surface rhodium atoms is compatible only with the presence of a reaction route that permits the removal of a couple of near oxygens at θ_O=0.5 ML.

We have checked, by means of DFT calculations of energy barriers, various possible pathways for reactions involving oxygen and hydrogen on Rh(111). We have verified that production of hydrogen peroxide is improbable because this molecule is much higher in energy compared to a couple of adsorbed hydroxyls. In regime of high oxygen coverage, when Rh(111) surface is hydrorepellent, hydrogen peroxide is still 0.72 eV higher in energy than a couple of hydroxyls (by definition activation energy value is larger) and both the hydroxyls need to penetrate a double row to activate the reaction. Concurrent water formation instead has an activation barrier of 0.20 eV in our best estimate and can be activated without particular constraints on the position of starting OH.

The only route compatible both with experimental data and our calculations is the formation of a couple of near waters. Formation of a second OH, after almost barrier-less diffusion of the near first OH formed, through a sort of autocatalytical process that involves an intermediate similar to a water molecule, has a barrier of 0.27 eV (figure 3.25). In the regime of the approximations used and actual DFT accuracy for these kind of processes, it is

comparable with water formation barrier. When barriers are so similar other factors can determine selectivity among different pathways, for example the prefactor in Arrhenius formula or hydrogen sticking coefficient.

It has been verified that at high oxygen coverage H is less mobile than on a clean surface and this can help us to explain the different water production rates visible in figure 3.3 that show us a peak when we pass from a p(2×1) to a p(2×2).

Appendix A

Functionals

DFT states that, given the electronic density at the ground state (n_0), we can determine the energy spectrum of our system [25]. Kohn Sham theorems demonstrate existence and uniqueness of the solution, so we can formally define a functional $E[n_0]$ whose output is the total electronic energy at the ground state.

It is well known that the theorems do not give any practical indication to really solve the problem and so during the last years a lot of approximated functionals have been developed. They all differ for the exchange and correlation part of the energy and so we usually call these corrections exchange-correlation functionals:

$$E_{xc}[n_0] = T[n_0] - T_0[n_0] + E_{ee}[n_0] - E_{\text{Hartree}}[n_0] \tag{A.1}$$

where T is the kinetic energy, T_0 the non interacting kinetic energy, E_{Hartree} the Hartree energy and E_{ee} is the exact Coulomb repulsion.

A.1 LDA

Local Density Approximation and its improvement Local Spin Density Approximation (LSDA) are the first functionals that have been developed. Even

if the hype of research has moved to more advanced functionals (all the family of general gradient corrections, hybrid functionals, time dependent DFT) LDA is still used. The reasons of its success depend, not only in the ability to reproduce many important physical properties of matter, but are also due to the elegance and physical coherence of its definition, to the point where it is common between chemists call LDA calculations *ab-initio*.

In fact the general idea of LDA is to approximate exchange and correlation as the one generated by an uniform electron gas (jellium) with the idea that for periodic system, since the density is slowly varying, this could give correct results:

$$E_{xc}^{\mathrm{LSD}}\left[n_{\uparrow}, n_{\downarrow}\right] = \int d\mathbf{r} n\left(\mathbf{r}\right) \epsilon_{xc}^{\mathrm{unif}}\left(n_{\uparrow}\left(\mathbf{r}\right), n_{\downarrow}\left(\mathbf{r}\right)\right). \tag{A.2}$$

It has been proved surprisingly that many properties like energies are decently estimated by LDA even for not slowly varying density systems like small molecules. Moreover for chemical reasons, like for example adsorption energies and energy barriers LDA is still inaccurate and since the beginning of 90s many functionals based on gradient correction have been proposed. In our work it has been soon clear that for example GGAs give a better description of molecules respect to metal surfaces (LDA is still the reference in reticular constants).

In appendix B we'll also point that a set of techniques have been developed to improve band gaps in Density functional theory (by the way even the best DFT shouldn't be used to compute band gaps because Kohn-Sham eigenvalues have no physical meaning in that sense). The perfect or "divine functional" is far away and it is probable that a set of good functionals will be developed in the future, each one suitable on a class of systems, more than one valid everywhere.

A.2 GGA

We are going to describe briefly the general ideas of general gradient approximation (GGA) to the aim of pointing out defects of the functionals and particulary to better criticize the results of our calculations. Modern functionals, GGAs, hybrid and so on lack the precision and coherent definition of LDA. They are called empirical functionals because they are tuned varying a certain amount of parameters. Even if this choice can be justified, we should know where and why it is valid.

The general form of a GGA exchange-correlation functional is

$$E_{xc}^{\mathrm{GGA}}\left[n_{\uparrow}, n_{\downarrow}\right] = \int d\mathbf{r} f\left(n_{\uparrow}\left(\mathbf{r}\right), n_{\downarrow}\left(\mathbf{r}\right), \nabla n_{\downarrow}, \nabla n_{\uparrow}\right) \tag{A.3}$$

with the idea that adding a dependence upon density gradient we should increase accuracy. The functional we have chosen for our thesis work is PBE [51], that can be considered a simplified analytic form of PW91 [74], fitted in such a way to reproduce the same results and it is usually considered semi-empirical.

In comparison with LDA, GGA tends to improve total energies, atomization energies, energy barriers, and structural energy differences. It tends to expand bonds and so sometimes it overcorrects LDA, for example reticular constants of rhodium and platinum are larger both than experimental and LDA values. This happens because the form of f is a compromise between various needs. For example, it has been verified that GGAs behave better in the average of systems if we choose a form of f such as it reproduces LDA in the case where gradient is zero, even if this constraint is generally not compatible with the parameters that best fit simple molecules. For simple systems like molecules chemists nowadays use BLYP functionals or hybrid functionals with exact exchange Hartree-Fock contribution (see section B.1.1 at page 82.)

The major theoretical drawback of GGAs is that, generally speaking, a functional form that contains a gradient expansion does not respect the conservation of exchange-correlation hole[1], unlike LDA. Of course there are many tricks to enforce this constraint (*e.g.* real space cut-off), but it is a general idea behind functionals that what works, even if tricky and dirty, should be preferred in any case to something more elegant but useless. For example one of the reasons for the more simplicity in analytical form of PBE, respect to PW91, is the renounce to some constraints that are physically important but computationally irrelevant, such as second order asymptotic limit for gradient expansion in the regions where density is slowly varying.

What instead is really important to notice is that, even if it has been verified that PW91 (or PBE) strongly increases precision in energy barriers for surface calculations (because there is a compromise in describing quite good both metal and molecules), we have no real guarantees that transition state energies are well computed. In fact functionals are fitted and tested in the region where atoms are far apart or bound. In the intermediate regions, such as in transition states, we have no guarantees of the accuracy. Even if experience suggests us to trust at least trends, we should remember that transition states energies could be overestimated or underestimated by default.

A.3 Dispersion forces

It is considered one of the most important open problems in density functional theory that, by definition, the functionals used cannot predict and estimate dispersion or *weak* forces, such as the Van der Waals that, particularly for the water molecule we have studied, could be of a certain relevance in adsorption energies. Many other water molecule's properties (*e.g.* geome-

[1] see section B.1.1 for a definition of exchange - correlation hole

try) are independent by the choice of GGA because in those cases dispersion forces are marginal [75].

Van der Waals interaction is a quantum-mechanical phenomenon originated from the interaction between instantaneous fluctuating dipoles. It exists even between two neutral systems without the overlap of electron density. But all the functionals developed involve only density and its gradient, so the long range van der Waals potential is missing. Probably only time-dependent DFT could in future give a complete description of dispersion forces, even if the research is active also in traditional DFT.

Between the techniques proposed we remember DFT plus dispersion, in which the short term part is computed in the standard way, while the long range part of the energy is computed with perturbation theory in multi-polar expansion. A simple and promising technique [76] is obtained by adding a correction term to the energy computed semi-empirically. All these methods have been tested on couples of molecules, such as rare gas dimers or benzene dimers, that constitute the reference for both theoretical modeling and experimental measurements of the van der Waals force. The improvements achieved do not yet guarantee the so-called chemical accuracy necessary to consider ab-initio calculations predictive.

Appendix B

PWSCF development

In this chapter we will briefly describe the development of some routines that allow efficient calculation of several quantities in our code (PWscf [24]), exploiting the locality of pseudopotential projectors and augmentation charges, by using a grid in real space, instead of the G-space one.

This was motivated by the need, in the currently under development, implementation of hybrid functionals (containing a fraction of exact HF exchange), of repeatedly calculating some integrals related to pseudopotentials, thus requiring their very efficient evaluation. I have been developing these routines till early months of 2006 and all the comments and technical issues refer in main part to what I have written. Successive changes or expansions are not treated. This part of the code has been developed by me and Stefano De Gironcoli and is now maintained by Carlo Sbraccia. All the code commented here is contained in the files exx.f90 and realus.f90 of current Quantum ESPRESSO distribution [24]. Technical details described are intended also as a guide for future developers and refer directly to the present implementation of the algorithms in PWscf.

B.1 Exact exchange

The theoretical formulation of density functional theory states that the energy is a functional of the electron density, which contains all the information we need to solve the problem. Indeed the practical algorithm, in use nowadays, introduce Kohn - Sham equations where wave functions are computed. We can use these wave functions to estimate exchange-correlation energy and so define an extended class of functionals called *implicit functionals*. It is important to remember that Kohn - Sham wave functions are only the eigenstates of Kohn Sham equation and not the real wave functions of the ground state. The simplest implicit functional is the exact exchange functional (EXX), that has no correlation and exchange given by the standard Fock term.

B.1.1 Hybrid functionals

EXX is not only useful for calculating a pure Hartree-Fock energy from Kohn Sham orbitals, but can be used to improve the performances of modern functionals. There is a class of recently developed functionals, called hybrid, because they literally mix a density functional part and an exact-exchange part. The exchange-correlation energy can be written as [25]

$$E_{xc} = \int d\mathbf{r} n\left(\mathbf{r}\right) \epsilon_{xc}\left(\left[n\right], \mathbf{r}\right) \tag{B.1}$$

where $\epsilon_{xc}\left(\left[n\right], \mathbf{r}\right)$ is an energy per electron at point $\mathbf{r}$ that depends only upon the density $n\left(\mathbf{r}, \sigma\right)$ in some neighborhood of point $\mathbf{r}$.

The existence of such a functional is guaranteed by the Kohn Sham theorems. A more operative definition leads to the so called coupling constant integration formula. In this model we can gradually switch on the electronic charge from zero (the non interacting case) to the real case through the values of the coupling constant λ. We impose that during the process the density

is kept constant. The change in energy is given by

$$\begin{aligned} E_{xc}[n] &= \int_0^{e^2} d\lambda \langle \psi_\lambda | \frac{dV_{\text{int}}}{d\lambda} | \psi_\lambda \rangle - E_{\text{Hartree}}[n] \\ &= \frac{1}{2} \int d^3 r n(\mathbf{r}) \int d^3 r' \frac{\bar{n}_{\text{xc}}(\mathbf{r} - \mathbf{r}')}{|\mathbf{r} - \mathbf{r}'|} \end{aligned} \tag{B.2}$$

that defines the coupling-constant-averaged hole $\bar{n}_{\text{xc}}(\mathbf{r} - \mathbf{r}')$

$$\bar{n}_{\text{xc}}(\mathbf{r} - \mathbf{r}') = \int_0^1 d\lambda n_{\text{xc}}^\lambda (\mathbf{r} - \mathbf{r}'). \tag{B.3}$$

If we compare (B.1) and (B.2) we derive

$$\epsilon_{xc}([n], \mathbf{r}) = \frac{1}{2} \int d^3 r' \frac{\bar{n}_{\text{xc}}(\mathbf{r} - \mathbf{r}')}{|\mathbf{r} - \mathbf{r}'|} \tag{B.4}$$

which shows that the exact exchange-correlation energy can be understood in terms of the potential energy due to the exchange correlation hole averaged over the interaction from $e^2 = 0$ to $e^2 = 1$. For $\lambda = 0$ we have the exact exchange energy. For $\lambda = 1$ we have DFT exchange-correlation energy, obtained through the chosen LDA or GGA approach. A first proposal to better estimate integral in equation (B.2) was to average the two values:

$$E_{\text{xc}} = \frac{1}{2} \left(E_x^{\text{HF}} + E_{\text{xc}}^{\text{DFA}} \right), \tag{B.5}$$

where with DFA we denote an LDA or GGA functional.

A successive more effective hybrid functional was proposed by Becke [77, 78] and called B3P91 because it uses three parameters and mixes the Hartree-Fock exchange, the exchange functional by Becke (B88) and the correlation from Perdew and Wang (PW91). It fits accurate results for many molecules. A more used functional is the B3LYP that instead uses the LYP correlation. This functional is defined by the formula

$$E_{\text{xc}} = E_{\text{xc}}^{\text{LDA}} + a_0 \left(E_x^{\text{HF}} - E_x^{\text{DFA}} \right) + a_x E_x^{\text{Becke}} + a_c E_c \tag{B.6}$$

with coefficients that are empirically adjusted to fit atomic and molecular data.

The coupling-constant integration approach has also been used to generate hybrid functionals by Perdew and coworkers, but with the idea of deriving the form theoretically. Based upon arguments on the variation of $E_{\mathrm{xc}}(\lambda)$ as a function of λ, Perdew, Ernzerhof and Burke [51] proposed the form

$$E_{\mathrm{xc}} = E_{\mathrm{xc}}^{\mathrm{LDA}} + \frac{1}{4}\left(E_x^{\mathrm{HF}} - E_{\mathrm{xc}}^{\mathrm{DFA}}\right), \tag{B.7}$$

that mixes in 1/4 the Hartree-Fock exchange energy.

Hybrid functionals can be used in different ways. The most striking change due to use of hybrid functionals is the predicted excitation energies; an example are the calculated bands of Si determined using the B3LYP functional, which as intermediate between LDA and Hartree-Fock are in general agreement with GW calculations [25].

B.1.2 EXX implementation

In PWscf EXX and hybrid functional are in development in the file exx.f90. Our reference has been the work made by Gygi and Baldereschi [79] with the aim of computing band gaps of silicon and other semiconductors. At first we have neglected US pseudopotentials and all the tests have been performed on atomic gas of hydrogen in a simple cubic cell varying the reticular constant. This not-realistic system is an useful benchmark since in the limit of infinite reticular constant we know the exact analytic solution of Fock equations.

The general expression for generic matrix element of Fock term in G-space is:

$$\langle \mathbf{k}+\mathbf{G}\left|H_{\mathrm{HF}}\right|\mathbf{k}+\mathbf{G}'\rangle = -\frac{4\pi e^2}{\Omega}\sum_{m,\mathbf{k}'}\sum_{\mathbf{G}''}\frac{c^*_{m\mathbf{k}'}(\mathbf{G}+\mathbf{G}')\,c_{m\mathbf{k}'}(\mathbf{G}+\mathbf{G}'')}{\left|\mathbf{k}-\mathbf{k}'-\mathbf{G}''\right|^2} \tag{B.8}$$

where we have used the decomposition of wave function in plane waves

$$\phi_{m\mathbf{k}}(\mathbf{r}) = \frac{1}{\sqrt{\Omega}}\sum_{\mathbf{G}} c_{m\mathbf{k}}(\mathbf{G})\, e^{\imath(\mathbf{k}+\mathbf{G}\cdot\mathbf{r})}. \tag{B.9}$$

There is a sum over all the bands and over all the $\mathbf{q} = \mathbf{k} - \mathbf{k}'$ points, so this calculation is at least an order of magnitude more expensive than the default electronic one that does not need an iteration over $\mathbf{k}'$. PWscf solves eigenvalues problem by iterative methods and so it is not necessary to compute all matrix elements but only the product between H and a generic wave-function. This is not only time consuming, but also space consuming, because we need to store all the intermediate wave-functions generated every time a matrix product is performed. It is preferable to store them in real space form. In fact expensive convolution products in a space are equivalent to Fourier transform of a simple product in the reciprocal one. PWscf uses this trick everywhere it is possible since a convolution product scales as N^2 while Fast Fourier Transform scales as $N \log N$. This leads to a huge amount of disk space, when the cell is large, all stored in a single file with exx extension, in such a way that, when the calculation is distributed through parallelization, every computational unit can have access to all the wave-functions. For instance tests performed on a 20 Bohr simple cubic hydrogen reticulum need 40 Gigabytes of space.

The sum in equation (B.8) contains a singularity for $\mathbf{k} - \mathbf{k}' - \mathbf{G}'' = 0$ that practically reduces to treat the case $\mathbf{q} = 0$. The singularity is originated from the $\frac{1}{r}$ form of Coulomb interaction. A first idea is to change the potential into some Yukawa or variation. The code contains the possibility to use a Yukawa potential

$$\langle \mathbf{k} + \mathbf{G} | H_{\mathrm{HF}} | \mathbf{k} + \mathbf{G}' \rangle = -\frac{4\pi e^2}{\Omega} \sum_{m,\mathbf{k}'} \sum_{\mathbf{G}''} \frac{c^*_{m\mathbf{k}'} (\mathbf{G} + \mathbf{G}') \, c_{m\mathbf{k}'} (\mathbf{G} + \mathbf{G}'')}{|\mathbf{k} - \mathbf{k}' - \mathbf{G}''|^2 + \mu^2} \tag{B.10}$$

with the desired μ, but it has been found preferable to threat the singularity through a technique developed by Baldereschi and Gygi [79]. In fact the fraction in equation (B.8) is decomposed into the sum of a regular part and

a not regular, but integrable, part:

$$\langle \mathbf{k}+\mathbf{G}\left|H_{\mathrm{HF}}\right|\mathbf{k}+\mathbf{G}'\rangle = -\frac{4\pi e^2}{\Omega}\left[\sum_{m,\mathbf{k}'}\left(\sum_{\mathbf{G}''}\frac{c^*_{m\mathbf{k}'}(\mathbf{G}+\mathbf{G}')c_{m\mathbf{k}'}(\mathbf{G}+\mathbf{G}'')}{|\mathbf{k}-\mathbf{k}'-\mathbf{G}''|^2}-\right.\right.$$
$$\left.\left.c^*_{m\mathbf{k}}\left(\mathbf{G}'\right)c_{m\mathbf{k}}\left(\mathbf{G}\right)F\left(\mathbf{k}-\mathbf{k}'\right)\right)\right] - \frac{4\pi e^2}{\Omega}\sum_{m,\mathbf{k}'}c^*_{m\mathbf{k}}\left(\mathbf{G}'\right)c_{m\mathbf{k}}\left(\mathbf{G}\right)F\left(\mathbf{k}-\mathbf{k}'\right). \tag{B.11}$$

If we choose a $F\left(\mathbf{k}-\mathbf{k}'\right)$ with the same singular behaviour of the potential, we can remove the singularity from the sum contained in square brackets. If the choice of F is appropriate, the remaining term can be analytically or numerically estimated, since we know that the singularity is integrable. Gygi suggests a function that is really useful for cubic lattices, but it is not general purpose oriented. We use a gaussian of the form

$$F_{\mathrm{Gauss}}\left(\mathbf{q}\right) = \sum_{\mathbf{G}}\frac{e^{-\alpha|\mathbf{q}+\mathbf{G}|^2}}{\left|\mathbf{q}+\mathbf{G}\right|^2} \tag{B.12}$$

that integrated gives the value of $2\alpha\left(\frac{\pi}{\alpha}\right)^{3/2}$.

Once we are in control of the singular behaviour of the sum, a reduced grid of $\mathbf{q}$ points, subset of the original one can be chosen to approximate the result. This results in an enhancement of performances because the number of FFTs required to calculate matrix product for EXX is consistently larger respect to standard functionals. So it is preferable to check for convergence versus $\mathbf{q}$ points grid and stop when the accuracy is sufficient. For some systems, even a single point in $\mathbf{q}$ grid is sufficient to reach a good accuracy.

US contribution to EXX has not yet been developed since involves the computation of several integrals related to augmentation charges. The routines now implemented to treat these quantities are expensive and we have concentrated to their improvement.

B.2 Real space ultrasoft

In actual standard implementation of PWscf all the calculations and integrals regarding augmentation charges, such the computation of D_{ij} [26] are made in G-space. This choice has some advantages, for example all quantities are translational invariant and forces on a simple periodic system (one atom in a box) are exactly zero. But the algorithms related are slow. For average size systems (a dozen of atoms) the routines that compute D_{ij} (newd) and that add the contribution of augmentation charges to the total density (addusdens) last for seconds, while in principle they could last few milliseconds. Similar calculations should be repeated dozens of time in each step of an exact exchange calculation, to add exchange contribution of augmented charge to the matrix element. Considering that the process is sufficiently slow, even without that term, techniques involving G-space could make it impracticable. Integrals of pseudo-potential quantities in R-space reduce to a sum over few points and are faster.

I have developed a set of routines, contained in the module realus, that permit to threat augmentation charges in real space and, as benchmark, i have reimplemented routines newd and addusdens in the new environment. The most expensive part of the calculations, comparable to the effort now necessary to call a single routine, is performed only when nucleii are moved, and all the data obtained (the values of Q and auxiliary variables) are stored for reuse. The driver routine, to be called every time we need to update variables, is qpointlist. Q is stored in our pseudo-potential file format in two ways: a tabular part and an analytical part. The tabular part is contained in the variable called qfunc, while the analytical part in the variable called qfcoef. Both contributions are stored in a radial mesh centered on the position of the atom and that they do not contain angular part. The mismatch between radial cells center on atoms and the grid of points in the crystal cell

determines all the numerical difficulties to treat augmentation charges in real space.

The first step consists in generating the list of cell points contained in the spheres. For each kind of atom we should consider two radii (analytical and tabular part of Q) and the larger defines the sphere of interest. We list the points of the cell mesh contained in the larger sphere, taking care of periodic replicas (this is implemented with a loop on all the 26 nearest-neighbour cells). The result is a set of points with coordinates referred to the crystal coordinates and distance from the atomic center, stored in the variables box and boxradius.

Qsave contains the values of Q_{ij} and is obtained multiplying the corresponding spherical harmonics by the radial part. The radial part is reconstructed considering the two different contributions. The analytical part is easily adapted to the cell mesh, because for each point we can compute the exact value. The tabuled part needs an interpolation. In the limit of a real dense mesh (high cutoff for charge density) the result is indipendent of the interpolation routine used. In practice the mismatch between radial and regular mesh results into a slight breaking of the translational invariance for energies. This means that residual forces are present even in highly symmetric systems. For large systems with many atoms, the errors tend to compensate but we desire high accuracy and compatibility with previous results.

We performed test calculations for platinum bulk, varying the position of the atom with respect to the center of the cell. Linear interpolation resulted to be the worst, causing unacceptable spurious fluctuations in the total energy of the order of 0.1 Ry. Cubic or spline interpolations lower this value within a few mRy, but only with a quartic interpolation we can reach consistency within mRy that can be otherwise achieved doubling cutoff for rho mesh (ecutrho). The high standards required by ESPRESSO project led us to

let real space calculations only optional, but for large systems it is certainly advisable to exploit this feature.

Bibliography

[1] J. W. Döbereiner. *Schweigg J.*, 39:1, 1823.

[2] J. J. Berzelius. *Jber. Chem.*, 15, 1837.

[3] K. J. Laidler. *Chemical kinetics*. Benjamin - Cummings, third edition, 1997.

[4] Gabor A. Somorjai. *Introduction to surface chemistry and catalysis*. John Wiley & Sons, Inc., 1994.

[5] P. Sabatier. *La Catalyse en Chimie Organique*. Bérange: Paris, 1920.

[6] M. Boudart. In G. Ertl, H. Knözinger, and J. Weitkamp, editors, *Handbook of heterogeneous catalysis*. Wiley-VCH, Weinheim, 1997.

[7] T. Bligaard, J. K. Nørskov, S. Dahl, J. Matthiesen, C. H. Christensen, and J. Sehested. The brønsted-evans-polanyi relation and the volcano curve in heterogeneous catalysis. *Journal of catalysis*, 224:206–217, 2004.

[8] J. K. Nørskov, T. Bligaard, A. Logadottir, S. Bahn, L. B. Hansen, M. Bollinger, H. Bengaard, B. Hammer, Z. Sljivancanin, M. Mavrikakis, Y. Xu, S. Dahl, and C. J. H. Jacobsen. Universality in heterogeneous catalysis. *Journal of catalysis*, 209:275–278, 2002.

[9] M. C. Desjonqueres and D. Spanjaard. *Concepts in surface physics*. Springer, 1995.

[10] S. Volkening, K. Bedurftig, K. Jacobi, J. Winterrlin, and G. Ertl. *Phys. Rev. Lett.*, 83:2672, 1999.

[11] S. Dahl, A. Logadottir, R.C. Egeberg, J. H. Larsen, I. Chorkendorff, E. Törnqvist, and J. K. Nørskov. Role of steps in N_2 activation on ru (0001). *Phys. Rev. Lett.*, 83:1814–1817, 1999.

[12] W. J. Here, L. Radom, P. v. R. Schleyer, and J. A. Pople. *Ab initio molecular orbital theory.* Wiley, New York, 1987.

[13] B. Hammer and J. K. Nørskov. Theoretical surface science and catalysis - calculations and concepts. *Advances in catalysis*, 45:71–129, 2000.

[14] B. Hammer and J. K. Nørskov. Electronic factors determining the reactivity of metal surfaces. *Surface science*, 343:211, 1995.

[15] P. J. Feibelman. Partial dissociation of water on ru(0001). *Science*, 295:99–102, 2002.

[16] A. Michaelides, V. A. Ranea, P. L. de Andres, and D. A. King. General model for water monomer adsorption on close-packed transition and noble metal surfaces. *Phys. Rev. Lett.*, 90(21), 2003.

[17] H. Ogasawara, B. Brena, D. Nordlund, M. Nyberg, A. Pelmenschikov, L. G. M. Pettersson, and A. Nilsson. *Phys. Rev. Lett.*, 89:276102, 2002.

[18] R. Ludwig. How does water bind to metal surfaces: Hydrogen atoms up or hydrogen atoms down? *Angew. Chem. Int. Ed.*, 42:3458–3460, 2003.

[19] K. D. Gibson, M. Viste, E. Sanchez, and S. J. Sibener. Physical and chemical properties of high density atomic oxygen overlayers under ultrahigh vacuum conditions: (1x1)-o/rh(111). *J. Chem. Phys.*, 112:2470–2478, 2000.

[20] G. Centi, R. Dittmeyer, S. Perathoner, and M. Reif. *Catalysis Today*, 79-80:139–149, 2003.

[21] Vasant R. Choudary, Abajii G. Gaikwad, and Sbhash D. Sansare. *Angew. Chem. Int. Ed.*, 40(9):1776–1779, 2001.

[22] V.R. Choudhary, S.D. Sansare, and A.G. Gaikwad. *Catalysis Letters*, 84(1-2):81–87, 2002.

[23] G. Centi and S. Perathoner. *Catalysis Today*, 79-80:3–13, 2003.

[24] S. Baroni, A. Dal Corso, S. de Gironcoli, and P. Giannozzi. http://www.pwscf.org ; see also http://www.quantum-espresso.org.

[25] Richard M. Martin. *Electronic structure Basic theory and practical methods*. Cambridge university press, 2004.

[26] D. Vanderbilt. *Phys. Rev. B*, 41:7892, 1990.

[27] M. Methfessel and A. Paxton. *Phys. Rev. B*, 40:3616, 1989.

[28] John P. Perdew, Kieron Burke, and Matthias Ernzerhof. Generalized gradient approximation made simple. *Phys. Rev. Lett.*, 77:3865, 1996.

[29] M. Levy and J. Perdew. *Density-Functional Methods in Physics*. Plenum, New York, 1985.

[30] Guido Fratesi. *Low temperature methane to methanol conversion on transition metal surfaces. An ab initio study.* PhD thesis, SISSA/ISAS - Trieste, 2005.

[31] Carlo Sbraccia. *Computer simulation of thermally activated processes. Theory, algorithms, and a few cases applications to surface chemistry.* PhD thesis, SISSA/ISAS - Trieste, 2005.

[32] J. Song, L. R. Corrales, G. Kresse, and H. Jonsson. Migration of o vacancies in α-quartz: The effect of excitons and electron holes. *Phys. Rev. B*, 64:134102, 2001.

[33] H. Jonsson, G. Mills, and K. W. Jacobsen. Nudged elastic band method. In B. J. Berne, G. Ciccotti, and D. F. Cohen, editors, *Classical and quantum dynamics in condensed matter phase simulations*, pages 385–404. World scientific, Singapore, 1998.

[34] C. Choi and R. Elber. *J. Chem. Phys.*, 94:751, 1991.

[35] G. Henkelman, B. P. Uberuaga, and H. Jonsson. A climbing image nudged elastic band method for finding saddle points and minimum energy paths. *Journal of chemical physics*, 113, 2000.

[36] L. Carrette, K. A. Friedrich, and U. Stimming. Fuel cells: Principles, types, fuels and applications. *CHEMPHYSCHEM*, 1:162–193, 2000.

[37] M. Sohrabi and A. Irandoukht. Synthesis and activity measurement of some water-gas shift reactions catalysts. *React. Kinet. Catal. Lett.*, 80:303–309, 2003.

[38] Wolfgang Ruettinger, Oleg Ilinich, and Robert J. Farrauto. A new generation of water gas shift catalysts for fuel cell applications. *Journal of Power Sources*, 118:61–65, 2003.

[39] D. A. Hickman and L. D. Schmidt. Production of syngas by direct catalytic oxydation of methane. *Science*, 259:343–346, 1993.

[40] P. J. Feibelman. *Phys. Rev. Lett.*, 91:59601, 2003.

[41] Sheng Meng, L. F. Xu, E. G. Wang, and Shivu Gao. *Phys. Rev. Lett.*, 89:176104, 2002.

[42] J.M. Smith and R. L. Palmer. *J. Chem. Phys.*, 56:13, 1972.

[43] A. B. Anton and D. C. Cadogan. *Surf. Sci.*, 239:L548, 1990.

[44] K. M. Ogle and J. M. White. *Surf. Sci.*, 139:43, 1984.

[45] J. L. Gland, G. B. Fisher, and E. B. Kollin. *J. Catal.*, 77:263, 1982.

[46] A. Michaelides and P. J. Hu. *Am. Chem. Soc.*, 123:4235, 2001.

[47] G. S. Karlberg, F. E. Olsson, M. Persson, and G. Whanstrom. *J. Chem. Phys.*, 119:4865, 2003.

[48] W. R. Williams, C. M. Marks, and L. D. Schmidt. *J. Phys. Chem.*, 96:5922, 1992.

[49] S. Wilke, V. Natoli, and M. H. Cohen. *J. Chem Phys.*, 112:9986, 2000.

[50] A. J. Kokalj. *Mol. Graphics Modelling*, 17:176, 1999. Code available from http://www.xcrysden.org/.

[51] J.P. Perdew, M. Ernzerhof, and K. Burke. Rationale for mixing exact exchange with density functional approximations. *J. Chem. Phys.*, 105:9982–9985, 1996.

[52] http://www.pwscf.org/pseudo/1.3/UPF/xxx, where xxx = Pt.pbe-n-van.UPF, H.pbe-rrkjus.UPF or O.pbe-rrkjus.UPF, for Pt, H, and O respectively.

[53] http://www.webelements.com/.

[54] W. S. Benedict, N. Gailer, and E. K. Plyler. *J. Chem. Phys.*, 24:1139, 1956.

[55] S. A. Clough, Y. Beers, G. P. Klein, and L.S. Rothman. *J. Chem. Phys.*, 59:2254, 1973.

[56] P.J. Feibelman, J. S. Nelson, and G. L. Kellogg. *Phys. Rev. B*, 49:10548, 1994.

[57] J. L. F. Da Silva, C. Stampfl, and M. Scheffler. *Surf. Sc.*, 600:703, 2006.

[58] Z. Crljen, P. Lazic, D. Sokcevic, and R. Brako. *Phys. Rev. B*, 68:195411, 2003.

[59] A. Kokalj, N. Bonini, C. Sbraccia, S. de Gironcoli, and S. Baroni. *J. Am. Chem. Soc.*, 126:16732, 2004.

[60] D. E. Ridler and M. V. Twigg. In M. V. Twigg, editor, *Catalyst Handbook*, pages 225–282. Wolfe Publishing: Frome, UK, 1989.

[61] A. Kokalj, A. Dal Corso, S. de Gironcoli, and S. Baroni. *J. Phys. Chem. B*, 106:9839, 2002.

[62] S. Lizzit, A. Baraldi, A. Groso, K. Reuter, M. V. Ganduglia-Pirovano, C. Stampfl, M. Scheffler, M. Stichler, C. Keller, W. Wurth, and D. Menzel. Surface core-level shifts of clean and oxygen-covered ru (0001). *Phys. Rev. B*, 63:205419, 2001.

[63] W. H. Weinberg. In C. T. Rettner and M. N. R. Ashfold, editors, *Dynamics of Gas - Surface interactions*. Royal Society of Chemistry, London, 1991.

[64] M. V. Ganduglia-Pirovano, M. Scheffler, A. Baraldi, S. Lizzit, G. Comelli, G. Paolucci, and R. Rosei. Oxygen-induced rh $3d_{5/2}$ surface core-level shifts on rh(111). *Phys. Rev. B*, 63, 2001.

[65] *Phys Rev B*, 48:7665–7667, 1993.

[66] *Phys rev B*, 40:3616, 1989.

[67] Monica Pozzo, Dario Alfè, Gianluigi Carlini, and Renzo Rosei. A comparative study of water dissociation on rh111 and ni111 studied with first principles calculations. *unpublished*, 2007.

[68] http://www.pwscf.org/pseudo/1.3/UPF/Rh.pbe-nd-rrkjus.UPF.

[69] G. Goor, W. Kunkel, and O. Weinberg. In *Ullmann's Encyclopedia of Industrial Chemistry*, volume A13, pages 443–466. VCH, Weinheim, 1989.

[70] O. v. Schickh. *Chem. Ing. Tech.*, 32:462–462, 1960.

[71] H. Henkel and W. Weber. *Chem. Abstr.*, 8:2463, 1914.

[72] http://srdata.nist.gov/cccbdb/.

[73] N.N. Greenwood and A. Earnshaw. *Chemistry of the elements*. Pergamon Press Ltd., 1984.

[74] J. P. Perdew. In P. Ziesche and H. Eschrig, editors, *Electronic structure of solids '91*. Akademie Verlag, Berlin, 1991.

[75] X. Wu, M. C. Vargas, S. Nayak, V. Lotrich, and G. Scoles. *J. Chem. Phys.*, 115:8748, 2001.

[76] Q. Wu and W. Yang. Empirical correction to density functional theory for van der waals interactions. *Journal of chemical physics*, 116:515–524, 2004.

[77] A. D. Becke. A new mixing of hartree-fock and local density-functional theories. *J. Chem. Phys*, 98:1372–1377, 1993.

[78] A. D. Becke. Density functional thermochemistry iii. the role of exact exchange. *J. Chem. Phys*, 98:5648–5652, 1993.

[79] F. Gygi and A. Baldereschi. Self-consistent hartree-fock and screened - exchange calculations in solids: Application to silicon. *Phys. Rev. B*, 34, 1986.

Acknowledgements

I am very grateful to Alessandro Baraldi for a critical reading of my thesis work. I really appreciated the nice collaboration we had for the studying of properties of rhodium surfaces. He has kindly provided all experimental data and some pictures. Work described in appendix B has been performed in collaboration with Stefano De Gironcoli, whom i thank for suggesting me those stimulating topics. I wish to thank also Tone Kokalji, Dario Alfè, Carlo Sbraccia for useful and interesting discussions. I thank SISSA for the possibilities, the resources and the freedom that has given me to develop in my personal studies, more or less related to physics.

I have really appreciated Stefano Baroni as supervisor and good buddy. It has been such a pity that most of the time we spent together was dedicated to discuss physics... :-)

I wish all the best to friends that have helped me in these years ... Giovanni Di Stasi, Francesca Chittaro, Sandra Gonzales, Mara Gandini and the wonderful Demian Battaglia. I cannot even forget Andrea "Genioz" Carloni, Giorgio "Iceman" Gazzola, Devis Abriani and expecially Marco "Mak" Bettiolo for the very good time we have spent together. I really thank Anthony Robbins, Tenzin "Dalai Lama" Gyatso and Daniel Goleman for their wonderful books that introduced me to NLP world.

Eine Umarmung zu meinem lieben Rhode.